Published in final edited form as:
Inorg Chem. 2012 August 6; 51(15): 8617–8628. doi:10.1021/ic3013766.

EPR/ENDOR, Mössbauer, and Quantum Chemical Investigation of Di-iron Complexes Mimicking the Active Oxidized State of [FeFe] Hydrogenase

Alexey Silakov[#,†], **Matthew T. Olsen**[+], **Stephen Sproules**[§], **Eduard J. Reijerse**[#], **Thomas B. Rauchfuss**[+], and **Wolfgang Lubitz**[#]

Alexey Silakov: aus40@psu.edu; Wolfgang Lubitz: wolfgang.lubitz@cec.mpg.de

[#]Max-Planck-Institut für Chemische Energiekonversion, Stiftstrasse 34–36, Mülheim a.d. Ruhr, 45470, Germany

[§]School of Chemistry and Photon Science Institute, The University of Manchester, Oxford Road, Manchester M13 9PL, U.K.

[+]Department of Chemistry, University of Illinois, A328 Chemical & Life Sciences Lab, 600 South Mathews Avenue, Urbana, IL 61801, USA

Abstract

Understanding the catalytic process of the heterolytic splitting and formation of molecular hydrogen is one of the key topics for the development of a future hydrogen economy. With an interest in elucidating the enzymatic mechanism of the $[Fe_2(S_2C_2H_4NH)(CN)_2(CO)_2(\mu\text{-}CO)]$ active center uniquely found in the [FeFe]-hydrogenases, we present a detailed spectroscopic and theoretical analysis of its inorganic model $[Fe_2(S_2X)(CO)_3(dppv)(PMe_3)]^+$ in two forms with S_2X = ethanedithiolate (**1edt**) and azadithiolate (**1adt**) (dppv =cis-1,2-bis(diphenylphosphino)ethylene). These complexes represent models for the oxidized mixed-valent Fe(I)Fe(II) state analogous to the active oxidized "H_{ox}" state of the native H-cluster. For both complexes, the ^{31}P hyperfine (HF) interactions were determined by pulse EPR and ENDOR methods. For **1edt**, the ^{57}Fe parameters were measured by ESEEM and Mössbauer spectroscopy, while for **1adt** ^{14}N and selected ^{1}H couplings could be obtained by ENDOR and HYSCORE. The spin density was found to be predominantly localized on the Fe(dppv) site. This spin distribution is different from the H-cluster where both the spin and charge density are delocalized over the two Fe centers. This difference is attributed to the influence of "native" cubane subcluster that is lacking in the inorganic models. The degree and character of the unpaired spin delocalization was found to vary from **1edt**, with an abiological dithiolate, to **1adt,** which features the authentic cofactor. For **1adt**, we find two ^{14}N signals, which are indicative for two possible isomers of the azadithiolate, demonstrating its high flexibility. All interaction parameters were also evaluated through density functional theory calculations at various levels.

Keywords

[FeFe] Hydrogenase; H-cluster; di-iron complexes; EPR; ENDOR; HYSCORE; Mössbauer

---

Correspondence to: Alexey Silakov, `aus40@psu.edu`; Wolfgang Lubitz, `wolfgang.lubitz@cec.mpg.de`.

[†] **Present Addresses** A.S. - Pennsylvania State University, Department of Chemistry, 104 Chemistry Building, University Park PA 16802

Supporting Information.
Extended experimental data on both **1edt** and **1adt**, details of the DFT calculations. This material is available free of charge via the Internet at http://pubs.acs.org.

INTRODUCTION

The most efficient method of storing energy is within a chemical bond. Molecular dihydrogen is touted as promising vessel for the storage of energy accumulated from renewable resources because of its low molecular weight and strong H–H single bond.[1–3] Nature has engineered hydrogenase enzymes that promote the (reversible) heterolytic formation of dihydrogen from two protons and two electrons, i.e.

$$H_2 \leftrightarrows H^- + H^+ \leftrightarrows 2H^+ + 2e^{-1,4,5}. \qquad (1)$$

Three classes of hydrogenases have been distinguished based on their active site metal constituents: [FeFe], [NiFe] and [Fe].[1,6]

The active center of [FeFe] hydrogenases, the “H-cluster”, is a complex 6Fe-cluster consisting of a “classical” four cysteine ligated [4Fe-4S] cluster appended to a catalytically active [2Fe] subcluster via a protein Cys-S ligand (see figure 1).[7,8] Both iron centers are coordinated by CO and CN^- ligands that stabilize low oxidation and spin states.[9,10] The two Fe ions are connected by a dithiolate bridge, whose central atom has sparked considerable debate since the available crystallographic data have insufficient resolution to discriminate O, C or N. [11,12] Convincing evidence for nitrogen as a central atom has been obtained from an extensive pulse electron paramagnetic resonance (EPR) study of the H-cluster. [12] It has been proposed that this moiety might serve as a well-positioned base for relaying protons to and from the iron center.[11–14]

Two catalytically relevant states of the H-cluster have been experimentally identified thus far.[1,10,15] The active oxidized state, "H_{ox}", is characterized by a formal 2+ charge on the cubane subunit and a Fe(I)-Fe(II) configuration of the [2Fe] sub-cluster (Figure 1). This state is believed to be the entry point of the catalytic cycle. Whether this state directly participates in the catalytic cycle or is merely a "ready" state depends on whether the exchangeable coordination site on the distal Fe is vacant (see figure 1). There is an indication that water completes the coordination sphere in this state, which must dissociate to permit substrate binding[16–18] (see below for the discussion of this ligation). Under reducing conditions e.g. provided by a hydrogen atmosphere or upon addition of a mild reductant the H_{ox} state converts into the so-called reduced state “H_{red}” which is EPR silent. Based on spectroscopic evidence, the valency of the binuclear subcluster is best characterized by Fe_p(I)-Fe_d(I),[19,20] although Fe_p(II)-Fe_d(0) is another conceivable assignment based on the study of model compounds.[21] In the H_{red} state the $[4Fe\text{-}4S]_H$ subcluster remains oxidized (formally $Fe(II)_2Fe(III)_2$).

Recently, we have provided evidence for another possible stable intermediate.[20] In this new state, the [4Fe-4S] presumably exists in the reduced $Fe(II)_3Fe(III)$ state. As it allows to store a second electron upon heterolytic splitting it is likely that during the catalytic cycle the H-cluster passes through this state.

The catalytically pertinent [2Fe] subcluster can be viewed as a semiclassical diiron complex embedded in the protein pocket as only the Cys-S of the cubane unit tethers the site covalently to the protein superstructure. Because the diiron center is so lightly attached to the protein, it has proven a tempting target for synthetic modeling studies directed toward developing artificial hydrogen conversion systems.[2,3] However, to date only few of the published model compounds show significant conversion of protons to H_2; the majority of cases requiring a substantial over-potential (i.e. the deviation of the mid-point potential from the ones observed for native systems). [3,23]

These deficiencies of current synthetic models are likely to arise from differences in the electronic structure between these models and the active site. Specifically, we have shown that the electronic structure of the native [2Fe] cluster is strongly affected by the presence of the [4Fe-4S] subcluster;[19] it is highly likely that this coupling is crucial for fine-tuning the electronic structure and thus the catalytic activity. Moreover, the pendant base, i.e. the bridging azadithiolate cofactor, might play an important role acting as a relay for proton transfer.[1,12–14,22,24,25] Understanding these aspects will provide important insight into the mechanisms of H_2 activating catalysts, ultimately underpinning the development of efficient synthetic catalysts. To date, however, our understanding of the electronic structure of the catalytically active part of the H-cluster is rather limited. Model compounds mimicking the [2Fe] site provide a convenient means to study this part of the active center separately from the cubane moiety.

Recently, we conducted a study of {2Fe3S} model compounds closely resembling the CO-inhibited oxidized state of the H-cluster, in which a CO ligand occupies the substrate binding site.[26,27] The electronic structure of these models features a strong delocalization of the spin density over both iron centers as well as some ligands. In contrast, our previous studies of the [FeFe] hydrogenase from *D. desulfuricans* indicated the spin density is localized on the proximal Fe in the H_{ox}-CO state.[19,28] This discrepancy was the first hint that the [4Fe-4S] subcluster significantly affects the electronic structure of the [2Fe] subcluster, despite the identical coordination sphere in the model and the enzyme.

In this work we present the first detailed EPR and Mössbauer study to elucidate the ground state electronic structure of biomimetic models resembling the dinuclear part of the active H_{ox} state of the H-cluster (Figure 1). Here we focus on the $[Fe_2(S_2X)(CO)_3(dppv)(PMe_3)]$ series of compounds, where dppv = cis-1,2-bis(diphenylphosphino)ethylene. In this class, the bridging dithiolate ligand can be varied considerably (X = $(CH_2)_2$; $(CH_2)_2CH_2$; $(CH_2)_2NH$; $(CH_2)_2O$; $(CH_2)_2NCH_2C_6H_5$). Although their redox processes are still far from the H_2/H^+ equilibrium potential (about −410 mV vs. NHE at pH 7), they nonetheless provide an accessible Fe(I)-Fe(II) mixed-valent analogue of the “native” H_{ox} state.

Two variants are studied, namely **1edt**: X = $(SCH_2)_2$ and **1adt**: X = $(SCH_2)_2NH$ (Figure 1). The structural properties of **1edt** have been well characterized in previous studies using various methods.[29–31] X-band continuous wave (CW) EPR spectra, showing an almost axial signal with a distinct 1:2:1 pattern originating from two equivalent ^{31}P nuclei of dppv, suggested the unpaired spin was confined to Fe_1 (coordinated by the dppv ligand) and hence formulated as Fe_2(II)-Fe_1(I). However, this result differed markedly from the fully delocalized description of the “native” H_{ox} state of the H-cluster.[19] This difference is analogous to the one found for the H_{ox}-CO state and the corresponding {2Fe3S} model compounds. [26,27]

The EPR spectrum of **1adt** is quite similar to that of **1edt** suggesting their electronic structures are similar as well. The deviation in the principal *g*-values must be a consequence of introducing an amine group into the dithiolate bridge. A similar picture emerges from the IR spectroscopic analysis of these compounds. The CO-stretching IR bands differ for the two compounds (**1edt**: ν_{CO} = 2015, 1962, 1887 cm^{-1}; **1adt**: ν_{CO} = 2013, 1956, 1901 cm^{-1}).[32]

In this work we examine the impact of the amine functionalized bridge on the distribution of spin density in the Fe(II)-Fe(I) state, and therein elucidate the ground state electronic structures of **1edt** and **1adt**. The aforementioned catalytic properties are then contrasted with the native enzyme whose electronic structure of the H_{ox} state has been previously examined by an extensive multifrequency EPR approach.[12]

Additionally, the present study investigates the applicability of density functional theory (DFT) to these model compounds. Although DFT methods are widely used for the investigation of [2Fe] low valent constructs[33] their performance was not yet fully tested against EPR data. Recently we have demonstrated that a hybrid functional in conjunction with moderately large basis sets afforded reasonable estimates of the experimental spin-Hamiltonian parameters of the H_{ox}-CO mimicks.[26,27] However, the present case is somewhat different because of the presumably localized nature of the spin density. It remains unclear whether DFT is suitable to track the impact of nuanced modifications to the second coordination sphere. In this work we use the obtained experimental data to address these points for the first time. The results of the theoretical studies were then also used to obtain further insight into the electronic properties of the studied models.

MATERIALS AND METHODS

EPR Spectroscopy

EPR measurements were performed on a setup based on Bruker ELEXSYS E 580 X- and Q-band spectrometers as described earlier.[19,28] For Q-band measurements we used a slightly overcoupled cylindrical TE011 homebuilt resonator.[34]

W-band ESEEM and HYSCORE measurements were performed on a Bruker ELEXSYS E 680 FT EPR W-band spectrometer with a helium flow cryostat and a variable-temperature TeraFlex Bruker resonator. The 84 GHz internal local oscillator source used for the W-band up/down converting unit was modified to achieve improved phase stability. The W-band bridge provided 300 mW output power. This setup allowed 24 ns as minimum length of the $\pi/2$ pulse using a critically coupled resonator.

The pulse sequences used in this work can be found in supplementary information (Figure S1). Conventional Q-band pulse ENDOR spectra were obtained using stochastic data acquisition[35] with one shot per point with $t_{mix} = 5$ µs. Variable mixing time ENDOR experiments were performed using the standard Davies and Mims ENDOR sequences in linear scan mode recording 20 – 50 shots per point. In all cases the shot repetition time was set to achieve an unsaturated ESE signal.

Pulse EPR data were simulated using home-written routines utilizing a conventional spin-Hamiltonian approach in the high field approximation as previously detailed.[26] In all simulations, the orientation selection was calculated accounting for the two strongly coupled ^{31}P nuclei. The ^{14}N quadrupole coupling constant was accounted for by the quadrupole coupling parameter (K), and asymmetry parameter (η):

$$K=2P_z=\frac{e^2qQ}{4I(2I-1)h}=\frac{e^2qQ}{4h},\eta=\frac{P_x-P_y}{P_z} \quad (2)$$

where P_x, P_y and P_z are the principal components of the traceless quadrupole tensor ($|P_x|\leq|P_y|\leq|P_z|$) and I is the nuclear spin.

Mössbauer Spectroscopy

Mössbauer spectra were recorded on an alternating constant acceleration spectrometer. The minimum experimental line width was 0.24 mm/s (full-width at half maximum). The sample temperature was maintained constant either in an Oxford Variox or an Oxford Mössbauer-Spectromag cryostat. The latter is a split-pair conducting magnet system for applying fields of up to 8 T to the samples that can be kept at temperatures in the range 1.5 – 250 K. The field at the sample is perpendicular to the γ beam. Isomer shifts are quoted relative to metallic iron at 300 K. Mössbauer spectra were simulated with a home-written spin Hamiltonian program based on the usual nuclear Hamiltonian formalism.[36]

DFT Calculations

All calculations were performed using the ORCA 2.8 software package[37] within the spin-unrestricted formalism. Geometry optimizations utilized the BP86 functional[38,39] in concert with Ahlrichs triple-ζ valence basis set with three sets of polarization functions (TZVPP) on all atoms including the hydrogen atoms.[40] The Ahlrichs (2df,2pd) polarization functions were obtained from the TurboMole basis set library under ftp.chemie.unikarlsruhe. de/pub/basen. The resolution of identity (RI) was used with the standard TZV/J expansion basis, as implemented in ORCA.

Calculations of spin-Hamiltonian parameters were performed using the three-parameter Becke–Lee–Yang–Parr (B3LYP) functional[41,42] with the Wachters basis set[43] on the irons and the TZVPP basis set on all other atoms. The calculated ^{57}Fe hyperfine coupling constants were obtained including second order spin-orbit coupling contribution. The calculated ^{57}Fe isomer shifts (δ) have been calibrated to the applied settings following previously published procedures.[44,45] The calibration ρ(0) values were obtained using the geometries presented by Romelt et al.[46] Correlation between the experimental isomer shifts δ (mm/s)[46] and calculated ρ(0) (a.u.$^{-3}$) follow the linear response $\delta = 0.1181 - 0.3821(\rho\ (0) - 11614)$, where 11614 a.u.$^{-3}$ has been added for convenience (see Supporting Information).

Single point energy calculations were obtained from both geometry optimization and spin-Hamiltonian calculations. However, since the differences in energies between different conformers are consistent between different types of calculations, here we only present those from the latter ones.

Synthesis of ^{57}Fe -Labeled Compounds

[^{57}Fe$_2$(S$_2$C$_2$H$_4$)(CO)$_6$]—This compound was prepared according to literature methods using isotopically enriched anhydrous $FeCl_2$.[31,47] A solution of $FeCl_2$ (0.26 g, 2.0 mmol) in 45 mL of acetone was treated with 1 atm of CO for 10 min. To the resulting yellow solution was added NEt_3 (0.30 mL, 22.0 mmol), changing the color to blue/grey. To this mixture was added $H_2S_2C_2H_4$ (0.1 mL, 10.6 mmol) generating a dark brown solution. The mixture was stirred for 15 minutes, at which point Zn powder (0.120 g, 1.9 mmol) was added. After 18 h, the red solution was filtered through a Celite plug, then dried in vacuo. The solid was reconstituted in CH_2Cl_2, and filtered through a silica plug. The solvent was stripped under vacuum and the residue extracted into hexane, and chromatographed on a plug of silica with hexane as eluent. Two bands were observed; the desired product as a large red band that eluted first, and a small pink band that was discarded. A small amount of brown insoluble material remained at the top of the column. The product fraction was dried in vacuo affording red crystals. Yield: 0.480 g (30%). This product was spectroscopically identical (^{1}H NMR, IR) to the non-enriched material.

[^{57}Fe$_2$(S$_2$C$_2$H$_4$)(CO)$_4$(dppv)]—Following published methods,[30] a slurry of 38% enriched [$^{57}Fe_2(S_2C_2H_4)(CO)_6$] (0.260 g, 7.2 mmol) and dppv (0.270 g, 6.8 mmol) in 10 mL of MeCN was treated with Me_3NO (0.065 g, 8.7 mmol), resulting in vigorous bubbling and a darkening of the solution. After 3 h, the supernatant was filtered off, and remaining precipitate was repeatedly recrystallized from CH_2Cl_2 by addition of five volumes of hexane until the supernatant was clear. Yield: 0.344 g (67%).

[$^{57}Fe_2(S_2C_2H_4)(CO)_3(dppv)(PMe_3)$]—This compound was prepared according to the literature recipe.[47] IR and ^{1}H NMR spectra of the product were identical to the non-enriched form. ^{31}P NMR (CD_2Cl_2): 95 (d, $J_{\text{Fe-P}}$ =53 Hz), 18 (d, $J_{\text{Fe-P}}$ = 47 Hz).

Sample Preparation

Synthesis of reduced versions of **1edt** and **1adt** followed the published procedures with minor modifications.[31,32] These compounds were dissolved in toluene to a final concentration of 2 – 4 mM, treated with 1 equivalent of Fc($BArF_4$) and stirred vigorously for 30 minutes under an inert atmosphere. Then the resulting material was transferred to quartz EPR tubes or Mössbauer teflon caps and frozen in liquid nitrogen.

RESULTS

Figure 2 shows EPR spectra of **1edt** and **1adt**, obtained by 2 pulse-ESE detected EPR at Q-band. Both samples show signals consistent with the presence of one dominant species. The [1:2:1] splitting patterns observed at X-band originating from two presumably equivalent ^{31}P nuclei of the dppv ligand[31] are washed out at Q-band because of the increased linewidth, however, the principal *g*-values are more clearly resolved. The **1edt** model shows a larger anisotropy and a smaller rhombicity of the *g*-matrix (g = 2.009, 2.028, 2.139), whereas the **1adt** is more rhombic but less anisotropic (g = 2.006, 2.030, 2.124). However, as the *g*-matrix of both complexes is rather axial, it is apparent that both compounds have similar electronic structures that are only modestly influenced by the bridge alteration.

1. Spectroscopic Results on 1edt

Although the two strong ^{31}P hyperfine interactions can already be partially resolved in CW EPR, these interactions were also probed using orientation-selected pulse ENDOR measurements. Q-band Davies ENDOR spectroscopy revealed two different sets of ^{31}P signals (Figure 3). One set corresponds to two strongly coupled ^{31}P nuclei of the *dppv* ligand consistent with the splitting observed previously in the X-band CW EPR spectra.[31] The best fit to the field dependent ENDOR signals was achieved assuming two slightly different ^{31}P HF couplings: $A(P_1) = (-72, -71, -80)$ MHz, $A(P_2) = (-73, -72, -85)$ MHz. In the lower frequency region we have detected another doublet, centered at the Larmor frequency of ^{31}P (ν_{31P} = 20.664 MHz at 1197.8 mT), which has been assigned to a weakly coupled ^{31}P nucleus, $A = (9.5, 11.0, 8.5)$ MHz. Results of the simulations of these spectra are summarized in Table 1. Since this ^{31}P HF coupling is much smaller than those from the dppv ligand, we conclude that it originates from the PMe_3 ligand at the second iron (Fe_2), indicating some delocalization of the spin density to this site.

As will become apparent below, the sign of this small ^{31}P HF coupling plays an important role in understanding the orientation of the PMe_3 ligand. To resolve the sign of this HF coupling we employed variable mixing time (VMT) ENDOR.[48,49] In this method the sign of the HC coupling in question can be directly read out from the polarization of the ENDOR signal upon increasing the delay time between the RF pulse and the detection sequence, t_{mix} (Figure S1), due to longitudinal electron spin relaxation. As can be seen from Figure 4, even at relatively high temperatures (25 K), we have observed an almost completely polarized Q-band ENDOR spectrum when t_{mix} exceeds 100 μs.

For S = ½ and I = ½, the frequency of the ENDOR resonances is given by

$$\nu_{\alpha(\beta)}=|-g_n\beta_n B_0+(-)A/2| \quad (3)$$

where g_n = nuclear g-value, β_n = nuclear magneton, B_0 = strength of magnetic field, A = the orientation-dependent HF coupling constant. Assignment of the ENDOR signals to a specific M_S manifold (α or β) enables the direct determination of the absolute sign of **A**. As follows from the description of VMT ENDOR experiments,[48–50] at sufficiently long delay time between the RF pulse and the detection (see Supporting Information for the pulse sequence), $t_{mix} \geq T_{1e}$, the ENDOR signal from the $M_S = -½$ (β-manifold) remains positive, while the $M_S = +½$ (α-manifold) signal decreases relative to the other signal and even changes its sign. Considering g_n values for ^{31}P and ^{1} H nuclei are positive a positive A would result in $\nu_\alpha < \nu_L = |g_n\beta_n B_0|$ and $\nu_\beta > \nu_L$ (see equation 3). In this case, the lower frequency component of the ENDOR doublet (i.e. ν_α) would be affected. However, in our experiment (Figure 4A) the opposite situation was observed indicating that $\nu_\alpha > \nu_L$. Thus $A(^{31}P, PMe_3)$ is *negative*. Despite being unable to simultaneously observe α-and β-manifold signals we can conclude that the ^{31}P(dppv) hyperfine couplings similarly have negative signs as the high frequency component of the ENDOR signal clearly decreases and becomes negative with increasing t_{mix} (Figure 4). In this experiment, a polarization of the ^{1}H signals has also been detected; however no definite assignment could be ascertained from the overlapping signals.

Although the observation of the weakly coupled ^{31}P nucleus indicates some degree of spin delocalization on to Fe_2, more direct insight into the electronic structure for these model compounds is obtained by a study of the iron centers themselves. Investigating the electronic environment of Fe atoms in coordination complexes and protein samples is routinely compromised by the absence of a nuclear spin of sufficient abundance. Naturally occurring ^{57}Fe (I =½) has a meager 2.2% abundance, so isotropic enrichment is necessary. In this project we benefit from the recently developed methods for the ^{57}Fe enrichment of **1edt**.[47] By a combination of Mössbauer and pulse EPR spectroscopic methods to these highly enriched samples, we obtained the ^{57}Fe HF coupling constants with high accuracy.

Applied field ^{57}Fe Mössbauer spectra of **1edt** measured at 4.2 K consist of two signals corresponding to the two Fe sites in the complex (Figure 5). One of the signals at 0.1 T represents a typical quadrupole doublet with HF coupling well hidden under the line width, thus indicating relatively weak ^{57}Fe HFI. The other contributing signal has a rather complex and broad shape even at low magnetic fields. The overall width of this signal remains invariant with increasing magnetic field. The spectral profile of this signal remains unchanged at 1.8 K eliminating the possibility for a strong relaxation case that could also result in considerable broadening of the spectra. We therefore conclude that this second contributor is subject to a relatively large and very anisotropic ^{57}Fe HF tensor.

Due to the complexity of the signal at all measured magnetic fields, no unique set of Mössbauer parameters could be unambiguously extracted. To increase the number of constraints and thus obtain a unique set of spin-Hamiltonian parameters, additional pulse EPR experiments were conducted on the ^{57}Fe labeled **1edt** sample.

The simulations exhibited in Figure 5 were obtained from a simultaneous fit of both Fe nuclei with the inclusion of fixed coupling parameters obtained from high-frequency ESEEM and HYSCORE data (vide infra). The ^{57}Fe-labeled **1edt** samples show distinct signals in the low frequency region of the Q- and W-band ESEEM spectra (Figure 6,7) that are consistent with a weakly coupled ^{57}Fe nucleus. Better resolution was obtained from HYSCORE measurements at Q-band frequency. The noticeable field dependence of these ^{57}Fe signals indicates a very anisotropic character of the HF coupling. The simulation could be performed using one set of parameters with a good fit to the experimental spectra (Figure 7). To corroborate these assignments we have also performed these HYSCORE experiments at W-band frequency (see Supporting Information). The resulting ^{57}Fe parameters match the Q-band data completely.

Concerning the second ^{57}Fe signal, as in the case of the Mössbauer data, the high frequency W-band ESEEM signals cannot be fit with a unique set of parameters. However, as Mössbauer and pulse EPR data impose different constraints, a simultaneous simulation of all the data (Q/W-band ESEEM and HYSCORE and Mössbauer) yielded a unique set of parameters of two ^{57}Fe HF couplings. Figures 6 – 7 include simulations obtained from this process. It is worth noting that this approach also allowed the identification of the sign of each ^{57}Fe HF coupling despite their pronounced anisotropy.

The ^{57}Fe HF coupling constants are consistent with the weakly coupled ^{57}Fe signals resolved in Mössbauer experiments. The W-band ESEEM spectra at selected field positions showed additional signals that could be attributed to a second strongly coupled ^{57}Fe nucleus. Figure 7 shows two field dependent series of 3-pulse ESEEM spectra obtained for two different τ-values. Based on these experiments, we can confirm that the spin density is predominantly located at Fe$_1$. However, as indicated by the presence of weakly coupled ^{57}Fe and ^{31}P nuclei, about 5 – 10% of the spin is found on Fe$_2$. Table 1 summarizes the ^{57}Fe and ^{31}P HF coupling parameters. Table 2 shows ^{57}Fe Mössbauer-specific parameters, extracted from the spectra.

2. Spectroscopic Results on 1adt

To assess the impact of a nitrogen atom in the dithiolate bridge (azadithiolate), we have pursued similar EPR investigations of **1adt** (Figure 1). Q-band ENDOR spectra of **1adt** displayed in Figure 8 were more intricate than those of its **1edt** counterpart (Figure 3). Aside from the strongly coupled ^{31}P signals, a distinct set of ^{1}H signals was observed (Figure 8B). The pattern with a splitting in the range 10 – 15 MHz remained centered at the ^{1}H Larmor frequency and unperturbed by variation in the magnetic field indicating a mostly isotropic HF coupling (Table 1). Tentatively, we attribute the observed ^{1}H signals to the methylene and/or amine protons of the azadithiolate moiety. This assignment is supported by DFT calculations, presented in the following section. Additional structure at the high frequency side of the proton range reveals ^{31}P signals, most clearly seen at the lowest measured magnetic field position (Figure 8B). These arise from two signals from either inequivalent nuclei of the dppv ligand or the presence of two isomeric forms of the complex.

In the low frequency region, the doublet at the ^{31}P Larmor frequency is assigned to the weakly coupled PMe$_3$ ligand (Figure 8A). Its field dependence (see Figure S3 in supplementary information) showed this coupling to be mostly isotropic. It is interesting to note that this ^{31}P HF coupling is significantly smaller in magnitude than for **1edt**.

From Q-band VMT (Davies) ENDOR experiments of **1adt** (Figure S4) we conclude that all ^{31}P signals (from PMe$_3$ and dppv) correspond to negative HF couplings, as for **1edt**. Conversely, the polarization pattern of the ^{1}H signals in Figure S4 identify the strongly coupled ^{1}H HF couplings as positive. Despite the lack of viable synthetic access to ^{57}Fe enriched variants of **1adt** that precludes similar ^{57}Fe Mössbauer and EPR studies as conducted on enriched **1edt**, it is nevertheless apparent from the ^{31}P(PMe$_3$) HF couplings that the electronic structure of **1adt** is distinct from that of **1edt**.

A combination of ESEEM and HYSCORE measurements enabled the determination of the HF and quadrupole coupling constants of the ^{14}N atom in the azadithiolate ligand as it is the only nitrogen in the system. However, the observed X-band HYSCORE spectra (Figures 9, S6) reveal rather complex ^{14}N signals. The majority of the signals in the (++) quadrant can be attributed to a single ^{14}N nucleus. Since the ridges in the HYSCORE spectra change considerably with the position of the magnetic field (Figure S6) we assume a highly anisotropic ^{14}N HF coupling. Closer examination of the spectra reveals additional signals that are most prominent in HYSCORE measurements with relatively short τ-values. These signals have a weaker magnetic field dependence and are attributed to a predominantly isotropic HF coupling.

Additional Q-band HYSCORE measurements produced two sets of signals as well (see Supporting Information). Spectral simulations depicted in Figure 9 yielded two distinct sets of ^{14}N HF parameters (Table 1). This observation can only be rationalized by attributing each HF coupling to one of two isomers of **1adt**, presumably arising from a bridge flip (eq 4). The almost identical magnitude of the quadrupole coupling for the observed ^{14}N signals corroborates this assignment (Table 3).

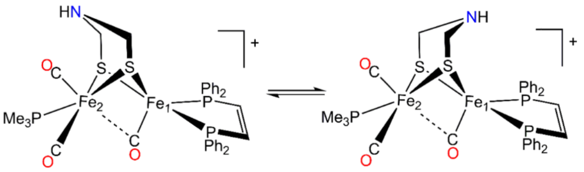

(4)

Although the geometry of the amine ligand in the model is presumably identical to that of the H-cluster, the measured ^{14}N quadrupole coupling in **1adt** is ~10% smaller than the one observed in the native enzyme (K(**1adt**) = 1.12/1.15 MHz versus $K(H_{ox})$ = 1.23 MHz).[12] We believe that this difference stems from the absence of neighboring protein residues that affect the site symmetry of the nitrogen atom in the enzyme.

3. Quantum chemical study of 1edt and 1adt

Previous studies of inorganic models of the H_{ox}-CO state, $[Fe_2(\mu\text{-}CO)(CO)_3(CN)_2(\text{dithiolate})]^{1-}$ (where dithiolate = $\{MeSCH_2C(Me)(CH_2S)_2\}$ (**2**)[26] or $\{MeS(CH_2)_2N(CH_2S)_2\}$ (**3**)[27]) produced calculated values in good agreement with the physical observables. However, while **2** and **3** show a highly delocalized spin density, the present compounds evidently produce a highly localized spin distribution.[31]

Based on geometry optimizations and earlier studies,[29,31] two principal geometric configurations of the ligands about Fe_1 in **1edt** are considered: (i) dithiolate and dppv ligands form a square-pyramidal arrangement with a semi-bridging position of the CO-ligand (designated as "flat"), and (ii) twisted arrangement of the dppv ligand with respect to the dithiolate bridge and CO in a terminal basal position and henceforth referred to as "twist" (Figure 10). For each of these two arrangements, two positions of the PMe_3 ligand at Fe_2 being apical (“ap”) or basal (“bas”) with respect to the dithiolate bridge are critical to the degree of spin delocalization in the molecule. An earlier X-ray crystallographic study of the reduced variant of **1edt** revealed an apical position of this ligand[29]. However, it should be noted that the conditions for sample preparation as well as the measuring conditions are different in the current case. As the formation of the crystal implies a tight packing of molecules, lattice forces might as well favor a different isomer. Hence, in this analysis we consider the four geometric alternatives shown in Figure 10A. Following the previous approach for **2** and **3**, i.e. spin unrestricted B3LYP-DFT calculations with all-electron valence triple-ζ basis sets (TZVP), the ^{31}P HF coupling constants for **1edt** and **1adt** were nicely reproduced. However, the correspondence between the experimental and computed ^{57}Fe HF coupling constants was less favorable. This situation did not improve using alternative popular hybrid functionals such as PBE0 and TPSSh nor by including a dielectric continuum.

The calculated ^{57}Fe A_{iso} values were found to be strongly affected by the basis set. Figure 11 presents the variation in ^{57}Fe A_{iso} values with the different basis sets used. TZVPP was maintained for all other atoms, having no substantial impact on the ^{57}Fe HF coupling constants. Surprisingly, we observed that depending on the flexibility of the core region of the iron basis sets the results fall into two distinct categories. The only exception is the rather large Atomic Natural Orbital (ANO) basis set Roos-ANO-TZP.[51] Illustrative of the overall sensitivity of the computed HF values to the basis set is the finding that a decontraction of a relatively small basis set SVP (indicated as "dec-SVP") leads to a completely different result, which is in fact much closer to the experiment.

Overall, the “Wachters” basis set [43] was preferred for computing the EPR and Mössbauer parameters; the data for **1edt** are given in Table 4. For calculations in vacuo, the energy differences between the various structures were found to be relatively small (<6 kcal/mol). Nevertheless, as expected based on the structural differences, the "flat" and "twist" conformations differ considerably in the spin density distribution (see supporting information, Figure S10). In the "flat" case, the spin density is predominantly localized on Fe_1, while it is delocalized over both Fe_1 and Fe_2 in the twisted isomers. The two classes of isomers also differ dramatically with respect to the electric field gradient constant on Fe_1. Given that a substantial quadrupole splitting is computed for the twisted isomers, we infer that only "flat" isomers are present in the measured samples in accord with the experimental quadrupole splitting.

Although the calculated magnitude of the ^{31}P HF coupling of the PMe_3 ligand is similar in the apical and basal conformations, its sign switches. This difference can be understood by considering that the spin density resides in a d_{z^2}-like orbital at Fe_2 and therefore the sign is positive for the position of the ligand along the axial direction of the d_{z^2} orbital (apical isomer) and negative in the equatorial plane of d_{z^2} orbital (basal isomer). Based on the sign determination using VMT ENDOR measurements, we conclude that the PMe_3 ligand in **1edt** is in the basal position. Although the crystal structure of **1edt** (as its BF_4^- salt) shows an apical PMe_3 in the solid, the structure of a related $Fe_2(pdt)(CO)_4(Imes)(PMe_3)]PF_6$ features basal PMe3 on Fe_2[52]. Our assignment is further corroborated by the fact that the "flat-bas" isomer has the lowest calculated single-point energy be it by only 2 kcal/mol [31]. Moreover, the spin density distribution mapped by DFT for the "flat-bas" isomer, with the unpaired electron essentially localized in a d_{z^2}-like orbital of Fe_1 with minimal delocalization to the other iron site, best matches the experiment. Knowing that we can reproduce the general electronic structure using DFT methods, we can now compare data for the **1edt** and **1adt** variants.

For **1adt**, we include two possible arrangements of the azadithiolate ligand as an additional degree of freedom. We will call the orientation of the amine facing the dppv ligand as "on", and the orientation to the other side as "off". We found that the overall electronic structure was insensitive to the orientation of the amine proton. In all cases examined, the amine proton projects toward the metal core as this afforded the most stable geometry. Additionally, we disregarded the "twist" isomer since the overall similarity in the EPR spectra of **1edt** and **1adt** implies that the "flat" isomer is dominant. Selecting only the “flat” arrangement for the dppv ligand, four isomers remain to be considered for **1adt** as depicted in Figure 10B.

We noticed that the position of the amine perturbs the arrangement of the dppv phenyl substituents; projection of the NH group into this space results in a minor tilt of the dppv ligand, which could explain the slight inequivalence of the two ^{31}P(dppv) hyperfine couplings. If the amine is flipped in the opposing direction, it affects the position of the PMe_3 ligand when this is in the apical position. Hence, the "off-ap" isomer has the highest calculated single-point energy. As was the case for **1edt** the negative sign of the PMe_3 ^{31}P HF coupling corresponds to a basal orientation of this ligand for **1adt**.

Concerning the orientation of the amine, the two experimentally extracted sets of ^{14}N HF coupling constants match the ones calculated for the “on” and “off” positions. If the nitrogen points towards the dppv ligand (and is closer to the spin density "cloud" near Fe) a large HF coupling constant is encountered. A much smaller ^{14}N HF coupling constant is obtained when the amine is pointing to the other side. Interestingly, only in the "off" isomers are the methylene protons of the dithiolate bridge (but not the amine proton) calculated to have relatively large HF couplings (Table 5). The sign of these ^{1}H HF coupling matches the experimental assignment. We therefore conclude that the two isomers of **1adt** detected in our experiments are "on-bas" and "off-bas".

Comparing the calculated values for these isomers with the experimental data we notice that the ^{1}H and ^{14}N HF coupling constants are considerably underestimated while the ^{31}P HF coupling for the PMe_3 ligand is highly overestimated. While for **1edt** the calculated ^{31}P HF couplings matched very well with the experimental results, the changes induced by the amino group in the bridging ligand, i.e. a reduction of spin density at Fe_1 with concomitant increase on the dithiolate bridge, were not as clearly reproduced in the calculations. However, the HOMO is indeed more distributed towards the dithiolate bridge in **1adt** than in **1edt** (Figure S10).

DISCUSSION

DFT accuracy

DFT calculations have reproduced the salient electronic structural features of the two models, **1edt** and **1adt** quite well. The calculated single-point energy differences between the various isomers are consistent with the experimental observations. The spin density was found to be localized on the five-coordinated Fe_1 site with some delocalization toward the six-coordinated Fe_2 site. A satisfactory agreement was also found for the ^{57}Fe Mössbauer parameters. Conversely, the calculated values of the ^{57}Fe HF coupling constants are strongly influenced by the flexibility of the basis set. This is not unexpected, but surprisingly, the dependence is not monotonic. Instead, two quite distinct cases were obtained with respect to the ^{57}Fe isotropic HF coupling constant for **1edt**. This apparently relates to two potential minima solutions that could be reached depending on the basis set core functions. This is a rather important finding since ^{57}Fe data provide critical insight into the electronic structure of diiron compounds and their reproducibility by DFT is crucial. Nevertheless, the analysis yields a logical trend: a larger basis set provides more accurate results. To verify, whether the same holds for the previously published models of the H_{ox}-CO state (**2**), we performed test calculations at the B3LYP level. Similarly, two different cases for the ^{57}Fe HF coupling could be achieved depending on the basis set (see Supporting Information). Quite interestingly, the completely opposite scenario arises, i.e. a *smaller* basis set provides a better fit to the experimental data than a large one. For **2**, the original standard contracted SVP basis set gives a very satisfactory agreement (see supporting information, Figure S9). Therefore, we conclude that despite the fact that the used methods can indeed reproduce the EPR parameters reasonably well, the DFT methods lack predictive power and for each state of the system the basis sets should be “tailored” to fit the experimental data. It remains to be seen if this problem is inherent to the DFT method or if further theoretical developments in DFT might come up with strategies to alleviate or circumvent this “bi-stability” effect.

A more subtle problem lies in the fact that the DFT methods did not identify electronic structural dissimilarities between **1edt** and **1adt**. According to the calculated spin Hamiltonian parameters, the electronic structures of these two compounds are virtually identical while experimentally there are obvious distinctions.

1edt vs. 1adt

Although a spin localized structure is adopted by both variants, subtleties in this distribution are evident in the spectroscopic analysis. From ^{57}Fe HF couplings in **1edt**, about 10% of the spin density is dispersed on Fe_2 which commutes with a substantial ^{31}P HF coupling constant of the PMe_3 ligand. Upon insertion of an amine the electronic structure changes. The ^{31}P (PMe_3) A_{iso} coupling decreases by a factor of three, attended by a loss of spin density from that ligand. We can exclude a conformational change from *basal* to *apical* because the sign of the HF coupling is retained. Furthermore the EPR spectrum of **1adt** is less anisotropic and more rhombic, corresponding to a modification of the frontier molecular orbital composition. The similar ^{31}P HF coupling of the dppv ligand underscores a nearly identical spin population on Fe_1 in **1edt** and **1adt**. Interestingly, the ^{1}H ENDOR spectra resolve strongly coupled methylene protons on the azadithiolate bridge in contrast to the case of **1edt**, where the methylene protons are much more weakly coupled. The PMe_3 ^{31}P hyperfine interaction in **1adt** is only one third of that in **1edt**. This would suggest that the azadithiolate bridge perturbs the charge distribution in the diiron core resulting in a decrease of the spin population on Fe_2 and a concomitant increase of the spin population on the dithiolate bridge. This accounts for the variation in electronic properties of the two dithiolates without amending the geometry. The steric and electronic impact of the amine functionality in the dithiolate bridge is expressed in the composition of the MOs in the Fe_2S_2 unit, and consistent with the ease with which **1adt** can be reduced.[31] Additionally, preliminary calculations suggested that the S–C bonding is affected by interactions with the nitrogen lone pair via the so-called anomeric effect, leading to enhanced coupling of the heteroatom with the Fe_2S_2 core.[53]

Comparison of 1adt with the H-cluster in the H_{ox} state

From the experimental and theoretical analysis, we conclude that the spin density in both studied variants is predominantly localized on Fe_1 with a moderate delocalization towards Fe_2. Thus it is clear that the models can be classed as Fe_1(I)-Fe_2(II) mixed valence compounds. This situation contrasts the previously studied model compounds **2** and **3** that resemble the H_{ox}-CO state, where the spin density is fully delocalized and integer oxidation states were not appropriate.[26] Thus, with saturation of the ligand environment on Fe_1 (i.e. binding of an additional CO ligand), the character of the unpaired spin density changes from localized to delocalized. An analogous trend was identified in the native H-cluster, wherein the spin density distribution was also found to shift towards the proximal iron upon CO inhibition of the H_{ox} state. However, there is a very significant difference between the actual spin distributions in the models and native system. In contrast to the model systems, the delocalized picture has been observed in the H_{ox} state and a localized one in the H_{ox}-CO state.

As previously detailed the electronic structure of the oxidized states of the H-cluster is heavily influenced by intercluster Heisenberg exchange interactions.[19,26] However, accounting for a Heisenberg spin-spin exchange mechanism alone seems insufficient to account for the discrepancy between the H_{ox} state and its inorganic mimic, **1adt**. Moreover, the exchange interaction is approximately 3–4 times weaker than in the H_{ox}-CO state and therefore the [4Fe-4S] cluster presumably has a minimal impact of the [2Fe] center. Contrarily, the DFT computed HOMO for the diiron unit is strikingly similar to those obtained for our model complexes,[12,18] and therefore we expect to see a localized spin density for the H_{ox} state. There could be several reasons for this discrepancy:

i. The coordination geometry of the H_{ox} state may deviate from the depiction given in Figure 1 owing to the inclusion of water in the vacant (sixth) coordination site of Fe_d, as inferred from crystallographic data of [FeFe] hydrogenase from *Clostridium pasteurianum* [7] and its recent refinement [17]. In recent DFT studies the presence of such a molecule has been shown to significantly affect the electronic structure [12,18]. However, since the authors specify the use of the reductant dithionite in the crystallization buffer it is doubtful that under these conditions the H_{ox} state is dominant in the crystal. Moreover, low temperature illumination experiments argue against the presence of water at the vacant site (see arrow in Figure 1). Below 60 K, the external CO ligand can be photodissociated, regenerating the H_{ox} state, as indicated by IR and EPR measurements.[10,15,54,55] Such a conversion argues against binding water at the same site. It is worth noting that the CO-photodissociation was observed even at 8 K. Taking into consideration the compact arrangement of amino acids about the open coordination site, dissociation of a CO ligand and instantaneous binding of a water ligand would require substantial motional freedom of the protein matrix which is clearly unrealistic at these temperatures. Thus, it is very likely that no ligand is present at the sixth coordination site of the distal iron in the H_{ox} state.

ii. The interaction with the surrounding protein environment may have a substantial effect on the electronic structure of the H-cluster. Our recent DFT calculations showed a surprisingly small influence of the protein matrix on the spin distribution in the H-cluster,[18] though Szilagyi et al. reported the opposite effect on the spin populations by including key acid residues.[56] Unfortunately, these results raise more questions about the reliability of such calculations on spin-exchange coupled Fe-cofactors such as the H-cluster. However, as the bi-nuclear cluster is a "dangling" unit with only one covalent bond to the protein (i.e. the Cys-S bridge between the 2Fe and 4Fe4S subclusters) the protein matrix is expected to exert only a minor influence on the electronic structure of the H-cluster. Nonetheless, the influence of the protein on the electronic structure of the active site remains an important area of investigation.

iii. The distinctive electronic interaction between the [2Fe] and [4Fe-4S] subclusters seems to be the most likely explanation for the differences between the model systems and the H-cluster. It clearly transcends a simple Heisenberg exchange approximation, as this would not result in a redistribution of the spin density in the bi-nuclear subcluster.[57,58] Increasing the exchange interaction merely attenuates the observable spin population of the [2Fe] subcluster, and the Heisenberg approach cannot accommodate alternative mechanisms such as double exchange. It would be interesting to study this phenomenon in more detail in model complexes featuring a second redox center thus mimicking the intracluster interaction in the H-cluster.

The properties of the amine in the dithiolate bridge is a further variable to consider in this system. It is apparent from the experimental data that two conformations of the adt ligand are probable, highlighting the flexibility of this bridge. A similar conclusion resulted from DFT calculations of the H-cluster,[17] where this flexibility may be pivotal in modulating catalytic rates as it relays protons during turnover. A recently synthesized family of $[Ni(diphosphine)_2]$ catalysts exploit the flexibility of the pendant base throughout the catalytic cycle.[25]

CONCLUSIONS

A detailed EPR and Mössbauer study of two structural di-iron models for the H_{ox} state of the H-cluster is presented. The spectroscopic data indicate that the ligand environment of the 1edt and 1adt models is characterized by a "flat" (dppv) and "basal" (PMe_3) configuration, which geometrically parallels the H-cluster. While the H_{ox} state of the H-cluster shows a delocalized spin density, the **1edt** and **1adt** are appropriately formulated as mixed-valent Fe_2(II)-Fe_1(I) pairs with the spin predominantly found on Fe_1 (in a $d_{z}{}^{2}$-like orbital). Inserting an amine into the dithiolate bridging ligand, i.e. going from **1edt** to **1adt**, pushes spin density away from Fe_2 towards the adt ligand accompanied by large HF couplings of the methylene protons and a measureable hyperfine and quadrupole interaction of the ^{14}N at the apex of the bridge. The adt ligand exhibits conformational flexibility leading to two configurations ("on" and "off"). DFT calculations corroborate the general picture derived from the experimental data. The ligand HF interactions (^{31}P, ^{1}H, ^{14}N) are well reproduced, but the properties calculated for the iron core, i.e. the ^{57}Fe HF interactions, are highly dependent on the chosen basis set. Finally, the calculated spin-density distribution was found to be essentially the same for **1edt** and **1adt**, which is not evident in the experiment.

This study provides valuable insight into the electronic and structural properties of the presented model systems. The differences between the resolved spectroscopic parameters of **1edt** and **1adt** and those obtained for the H-cluster underscore the difficulty in reproducing the precise electronic environment programmed into the native system with all parts playing an important role in tuning this efficient hydrogen catalyst for the best performance.

Supplementary Material

Refer to Web version on PubMed Central for supplementary material.

Acknowledgments

We are grateful to Dr. E. Bill for many useful discussions, and to B. Mienert, G. Klihm and F. Reikowski for their technical expertise and invaluable assistance during the experiments.

Funding Sources

This work was financially supported by the EU/Energy Network project SOLAR-H2 (FP7 contract 212508) and National Institutes of Health (GM061153).

REFERENCES

1. Lubitz W, Reijerse E, van GM. Chem Rev. 2007; 107(10):4331–4365. [PubMed: 17845059]
2. Barton BE, Olsen MT, Rauchfuss TB. Curr. Opin. Biotechnol. 2010; 21(3):292–297. [PubMed: 20356731]
3. Tard C, Pickett CJ. Chem Rev. 2009; 109(6):2245–2274. [PubMed: 19438209]
4. Cammack, R.; Frey, M.; Robson, RL. Hydrogen as a fuel: learning from nature. Taylor & Francis; 2001.
5. Lubitz W, Tumas W. Chem. Rev. 2007; 107(10):3900–3903. [PubMed: 17927154]
6. Salomone-Stagni M, Stellato F, Whaley CM, Vogt S, Morante S, Shima S, Rauchfuss TB, Meyer-Klaucke W. Dalton Trans. 2010; 39(12):3057–3064. [PubMed: 20221540]
7. Peters JW, Lanzilotta WN, Lemon BJ, Seefeldt LC. Science. 1998; 282(5395):1853–1858. [PubMed: 9836629]
8. Nicolet Y, Piras C, Legrand P, Hatchikian CE, Fontecilla-Camps JC. Structure. 1999; 7(1):13–23. [PubMed: 10368269]

9. Pierik AJ, Hulstein M, Hagen WR, Albracht SP. Eur. J Biochem. 1998; 258(2):572–578. [PubMed: 9874225]
10. Albracht SP, Roseboom W, Hatchikian EC. J Biol. Inorg. Chem. 2006; 11(1):88–101. [PubMed: 16323020]
11. Nicolet Y, de Lacey AL, Vernede X, Fernandez VM, Hatchikian EC, Fontecilla-Camps JC. J Am Chem Soc. 2001; 123(8):1596–1601. [PubMed: 11456758]
12. Silakov A, Wenk B, Reijerse E, Lubitz W. Phys. Chem Chem Phys. 2009; 11(31):6592–6599. [PubMed: 19639134]
13. Fan HJ, Hall MB. J Am Chem Soc. 2001; 123(16):3828–3829. [PubMed: 11457119]
14. Barton BE, Olsen MT, Rauchfuss TB. J Am Chem Soc. 2008; 130(50):16834–16835. [PubMed: 19053433]
15. Roseboom W, de Lacey AL, Fernandez VM, Hatchikian EC, Albracht SP. J Biol. Inorg. Chem. 2006; 11(1):102–118. [PubMed: 16323019]
16. Nicolet Y, Lemon BJ, Fontecilla-Camps JC, Peters JW. Trends Biochem. Sci. 2000; 25(3):138–143. [PubMed: 10694885]
17. Pandey AS, Harris TV, Giles LJ, Peters JW, Szilagyi RK. J. Am. Chem. Soc. 2008; 130(13):4533–4540. [PubMed: 18324814]
18. Greco C, Silakov A, Bruschi M, Ryde U, De Gioia L, Lubitz W. Eur. J. Inorg. Chem. 2011; (7): 1043–1049.
19. Silakov A, Reijerse EJ, Albracht SP, Hatchikian EC, Lubitz W. J Am Chem Soc. 2007; 129(37): 11447–11458. [PubMed: 17722921]
20. Silakov A, Kamp C, Reijerse E, Happe T, Lubitz W. Biochemistry. 2009; 48(33):7780–7786. [PubMed: 19634879]
21. Cheah MH, Tard C, Borg SJ, Liu X, Ibrahim SK, Pickett CJ, Best SP. J. Am. Chem. Soc. 2007; 129(36):11085–11092. [PubMed: 17705475]
22. Olsen MT, Rauchfuss TB, Wilson SR. J Am Chem Soc. 2010; 132(50):17733–17740. [PubMed: 21114298]
23. Tschierlei S, Ott S, Lomoth R. Energy & Environmental Science. 2011; 4(7):2340–2352.
24. Nicolet Y, Cavazza C, Fontecilla-Camps JC. J Inorg. Biochem. 2002; 91(1):1–8. [PubMed: 12121756]
25. Yang JY, Chen ST, Dougherty WG, Kassel WS, Bullock RM, Dubois DL, Raugei S, Rousseau R, Dupuis M, Dubois MR. Chemical Communications. 2010; 46(45):8618–8620. [PubMed: 20938535]
26. Silakov A, Shaw JL, Reijerse EJ, Lubitz W. J Am Chem Soc. 2010; 132:17578–17587.
27. Erdem OF, Schwartz L, Stein M, Silakov A, Kaur-Ghumaan S, Huang P, Ott S, Reijerse EJ, Lubitz W. Angew. Chem Int. Ed Engl. 2011; 50:1439–1443. [PubMed: 21290530]
28. Silakov A, Wenk B, Reijerse E, Albracht SP, Lubitz W. J Biol. Inorg. Chem. 2009; 14(2):301–313. [PubMed: 19011912]
29. Justice AK, Rauchfuss TB, Wilson SR. Angew. Chem Int. Ed Engl. 2007; 46(32):6152–6154. [PubMed: 17615612]
30. Justice AK, Zampella G, De GL, Rauchfuss TB, van der Vlugt JI, Wilson SR. Inorg. Chem. 2007; 46(5):1655–1664. [PubMed: 17279743]
31. Justice AK, De GL, Nilges MJ, Rauchfuss TB, Wilson SR, Zampella G. Inorg. Chem. 2008; 47(16):7405–7414. [PubMed: 18620387]
32. Olsen MT, Barton BE, Rauchfuss TB. Inorg. Chem. 2009; 48(16):7507–7509. [PubMed: 19603776]
33. Siegbahn PEM, Tye JW, Hall MB. Chem. Rev. 2007; 107(10):4414–4435. [PubMed: 17927160]
34. Reijerse E, Lendzian F, Isaacson R, Lubitz W. J Magn Reson. 2012; 214:237–243. [PubMed: 22196894]
35. Epel B, Arieli D, Baute D, Goldfarb D. Journal of Magnetic Resonance. 2003; 164(1):78–83. [PubMed: 12932459]

36. Gutlich, P.; Bill, E.; Trautwein, AX. Mossbauer Spectroscopy and Transition Metal Chemistry: Fundamentals and Applications. Berlin: Springer-Verlag; 2011.
37. ORCA–an ab initio, Density Functional and Semiempirical Program Package, version 2.8.0. 2011
38. Perdew JP. Phys. Rev. B. 1986; 33(12):8822.
39. Becke AD. Phys. Rev. A. 1988; 38(6):3098. [PubMed: 9900728]
40. Schafer A, Horn H, Ahlrichs R. Journal of Chemical Physics. 1992; 97(4):2571–2577.
41. Lee CT, Yang WT, Parr RG. Phys. Rev. B. 1988; 37(2):785–789.
42. Becke AD. Journal of Chemical Physics. 1993; 98(7):5648–5652.
43. Wachters AJ. Journal of Chemical Physics. 1970; 52(3):1033.
44. Filatov M. Journal of Chemical Physics. 2007; 127(8)
45. Sinnecker S, Slep LD, Bill E, Neese F. Inorg. Chem. 2005; 44(7):2245–2254. [PubMed: 15792459]
46. Romelt M, Ye S, Neese F. Inorg. Chem. 2009; 48(3):784–785. [PubMed: 19102678]
47. Volkers PI, Boyke CA, Chen J, Rauchfuss TB, Whaley CM, Wilson SR, Yao H. Inorg. Chem. 2008; 47(15):7002–7008. [PubMed: 18610969]
48. Epel B, Poppl A, Manikandan P, Vega S, Goldfarb D. Journal of Magnetic Resonance. 2001; 148(2):388–397. [PubMed: 11237646]
49. Epel B, Niklas J, Antonkine M, Lubitz W. Applied Magnetic Resonance. 2006; 30(3–4):311–327.
50. Doan PE. Journal of Magnetic Resonance. 2011; 208(1):76–86. [PubMed: 21075026]
51. Roos BO, Lindh R, Malmqvist P-A, Veryazov V, Widmark PO. J. Phys. Chem. A. 2005; 109(29): 6575–6579. [PubMed: 16834004]
52. Liu T, Darensbourg MY. J. Am. Chem. Soc. 2007; 129(22):7008–7009. [PubMed: 17497786]
53. Lawrence JD, Li H, Rauchfuss TB, Benard M, Rohmer MM. Angew. Chem Int. Ed Engl. 2001; 40(9):1768–1771. [PubMed: 11353506]
54. Chen ZJ, Lemon BJ, Huang S, Swartz DJ, Peters JW, Bagley KA. Biochemistry. 2002; 41(6): 2036–2043. [PubMed: 11827551]
55. Silakov A, Reijerse EJ, Lubitz W. Eur. J. Inorg. Chem. 2011; (7):1056–1066.
56. Giles LJ, Grigoropoulos A, Szilagyi RK. Eur. J. Inorg. Chem. 2011; 2011(17):2677–2690.
57. Popescu CV, Munck E. J. Am. Chem. Soc. 1999; 121(34):7877–7884.
58. Pereira AS, Tavares P, Moura I, Moura JJG, Huynh BH. J. Am. Chem. Soc. 2001; 123(12):2771–2782. [PubMed: 11456963]

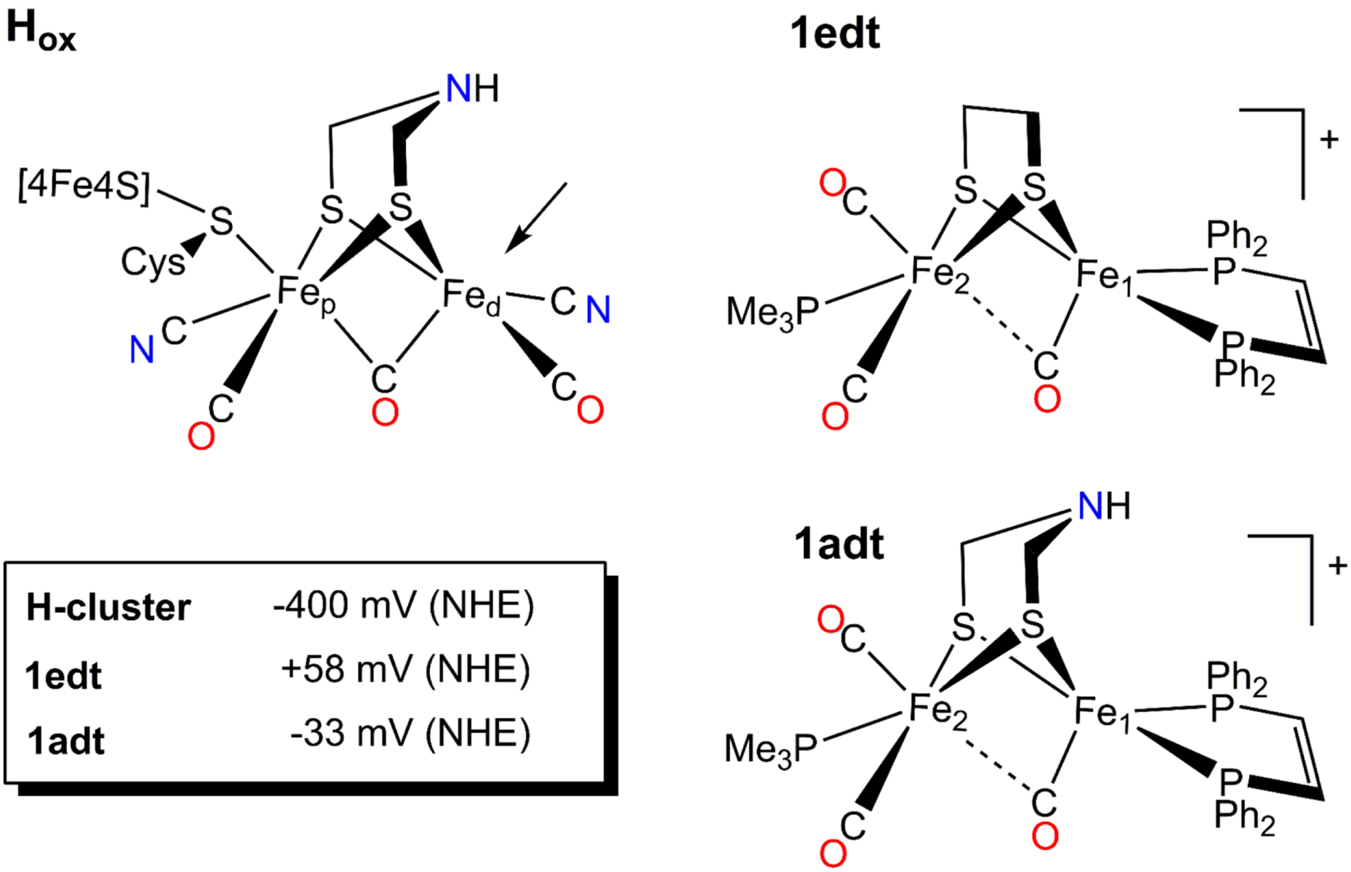

H-cluster	-400 mV (NHE)
1edt	+58 mV (NHE)
1adt	-33 mV (NHE)

Figure 1.

Schematic representation of the H-cluster in the H_{ox} state and model compounds used in this study. An Arrow points to the vacant apical site on the distal Fe, which in the case of the enzyme, is the site for binding H_2. Insert: midpoint potentials for the H_{red}/H_{ox} and $[Fe_2(SX)_2]^{0/+}$ redox transition for the H-cluster and the models 1edt and 1adt, correspondingly. For the H-cluster it is specified for pH 8 [15] in Tris buffer with KCl electrolyte, for the model compounds the E_0 values are given for $[(C_4H_9)_4N]PF_6$ electrolyte in CH_2Cl_2 [22] and values are converted from vs $Fc^{0/+}$ to vs NHE scale by using $E_0(Fc^{0/+})$ = +0.528 vs NHE estimation.

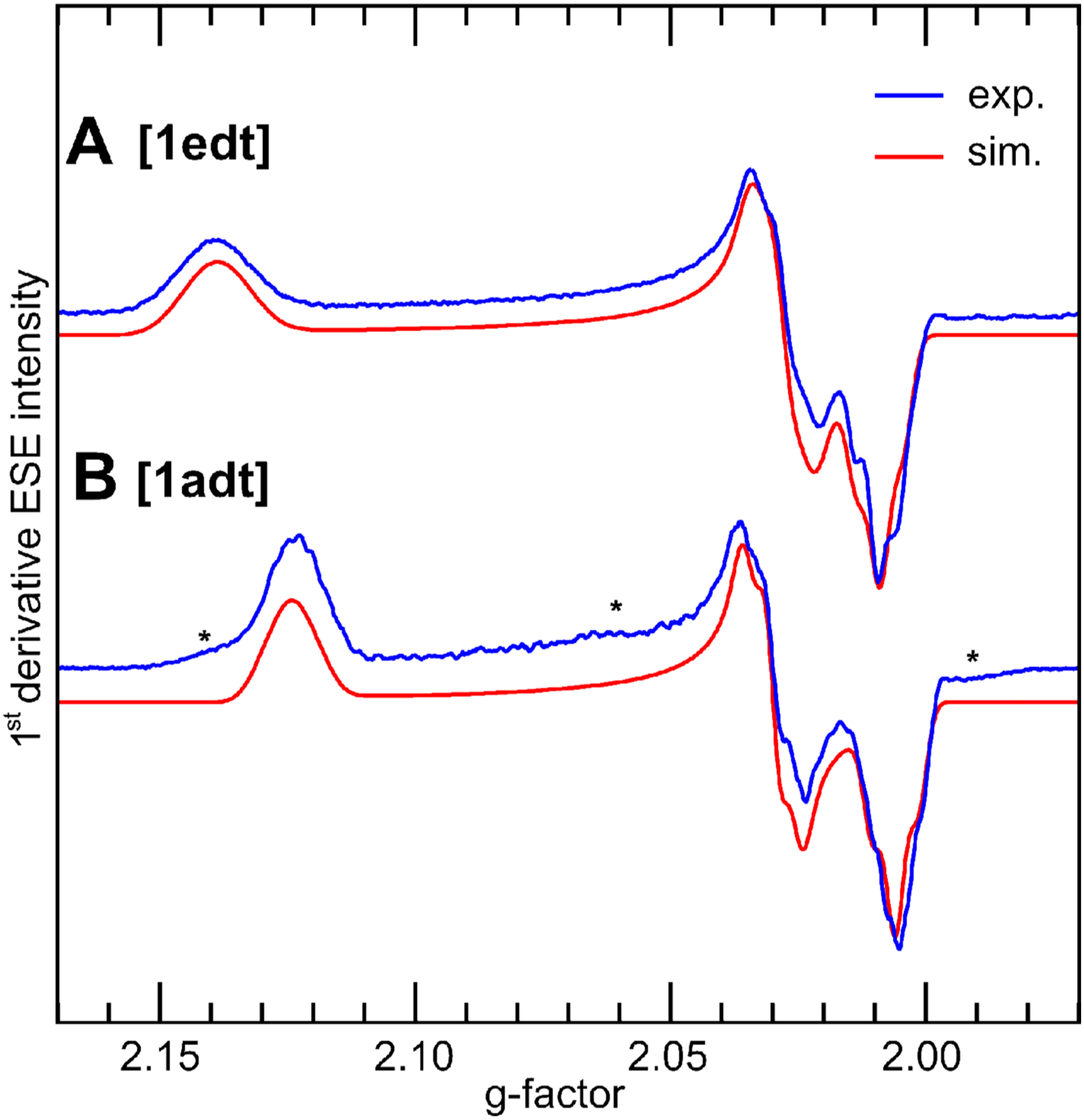

Figure 2.

First derivative (pseudomodulated) Q-band two pulse echo-detected EPR spectra (blue) of frozen solutions of **1edt** (**A**) and **1adt** (**B**) and corresponding simulations (red) using principal g-values: **A** g^{1edt}=(2.009, 2.028, 2.139), **B** g^{1adt}=(2.006, 2.030, 2.124). Experimental conditions: T = 20 K, ν_{mw} = 33.8560 GHz (**A**), 33.918 GHz (**B**), τ= 340 ns. The asterisks on **B** indicate minor contaminations of unknown origin.

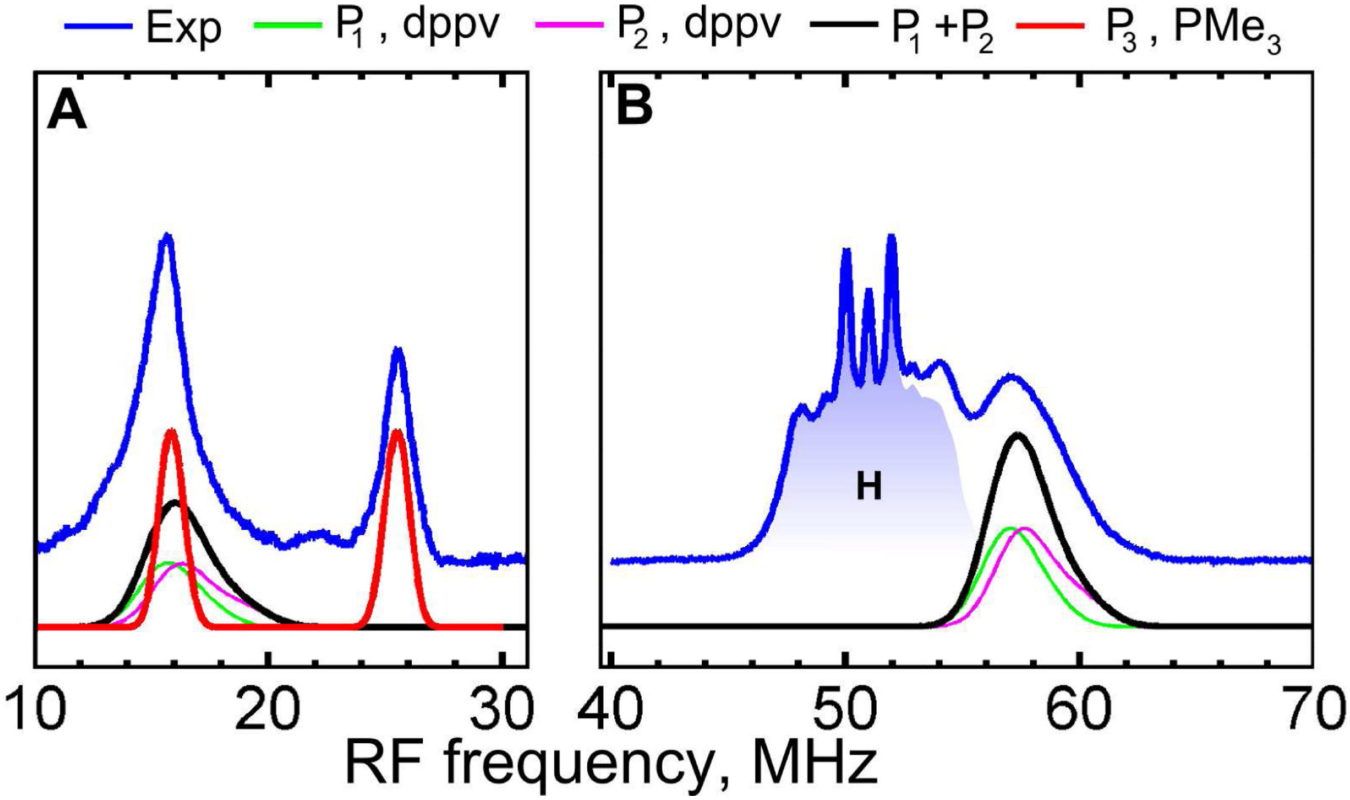

Figure 3.

Q-band Davies ENDOR spectra (blue) of **1edt** measured at T = 20K and 1197.8 mT. Simulations were performed using $P_{1,2,3}$ parameters from Table 1. The ^{1}H ENDOR region is shaded blue for clarity. Experimental conditions: **A**, t_{RF} = 35 μs; ν_{mw} = 33.8708 GHz; t_{inv} = 200ns. **B**, t_{RF} = 5.5 μs; ν_{mw} = 33.8708 GHz; t_{inv} = 80 ns; see also Figure S2 in SI for complete field dependence.

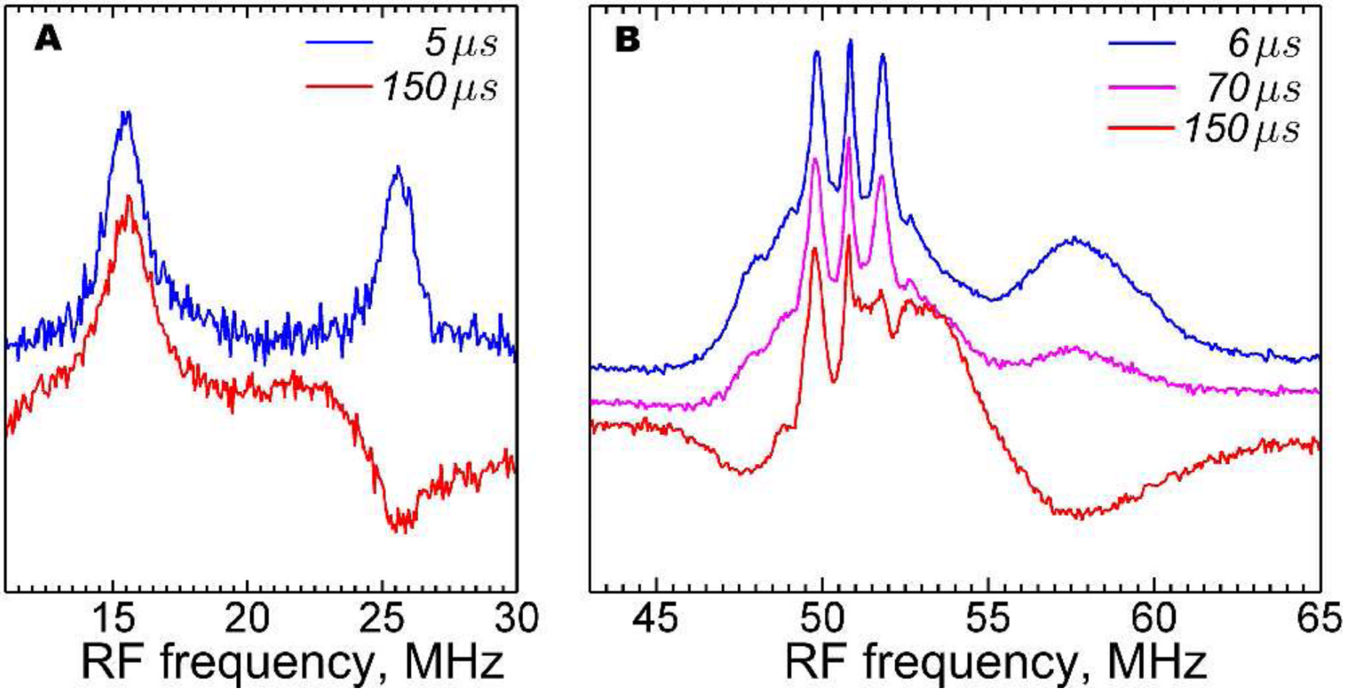

Figure 4.

Q-band VMT (Davies) ENDOR of **1edt** measured for various t_{mix} delay times (see SI) at maximum absorption of the EPR spectrum (g_y). Both low (**A**) and high (**B**) frequency ENDOR signals show a clear dependence on t_{mix} delay times (indicated in the figure). Experimental conditions: **A**, T = 25 K; t_{RF} = 20 μs; ν_{mw} = 33.8269 GHz; B_0 = 1192.3 mT; t_{inv} = 100 ns. **B**, T = 25 K; t_{RF} = 7 μs; ν_{mw} = 33.8865 GHz; B_0 = 1194.4 mT; t_{inv} = 80 ns.

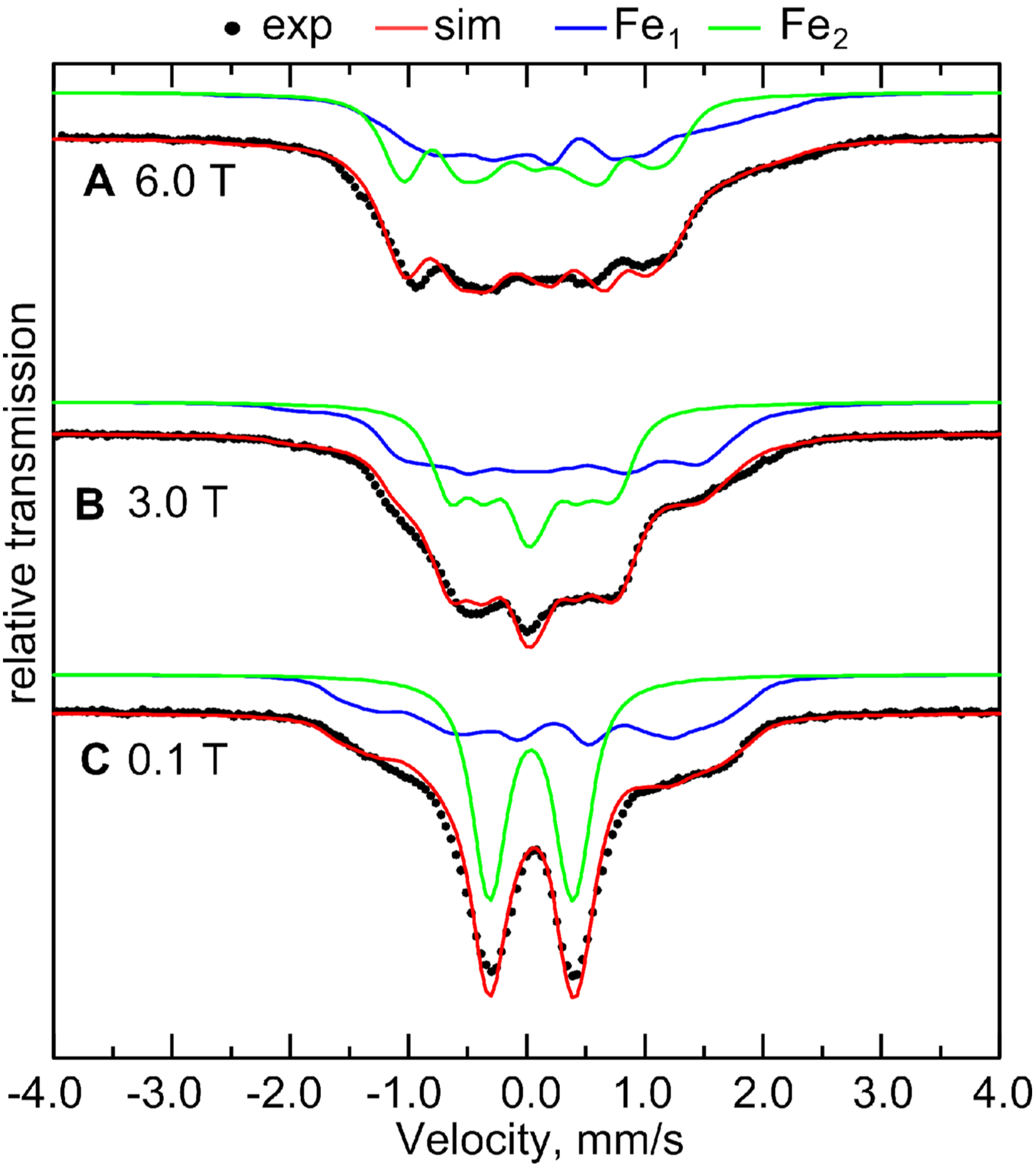

Figure 5.

Mössbauer spectra of the fully ^{57}Fe enriched **1edt** measured at three magnetic field strengths at a temperature of 4.2 K (black) and respective simulations (red) accounting for two contributing ^{57}Fe nuclei: Fe_1 (blue) and Fe_2 (green) with parameters presented in Tables 1 and 2.

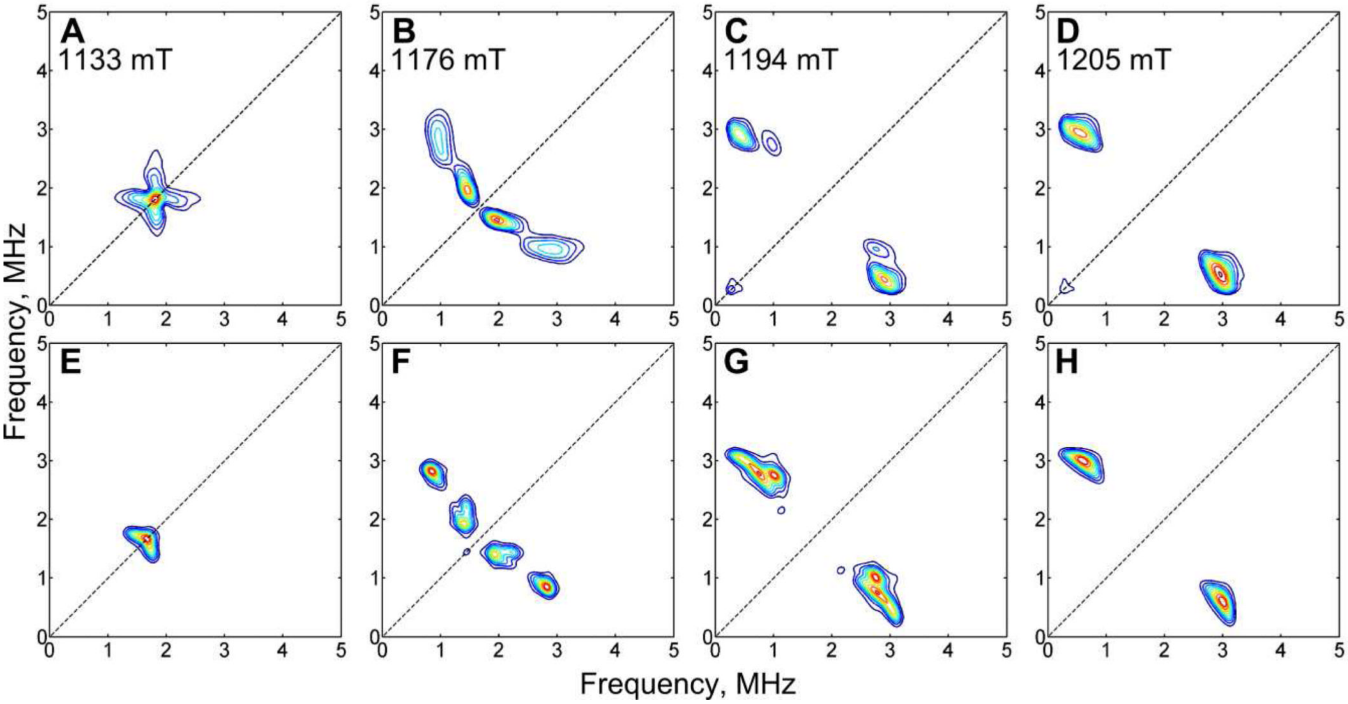

Figure 6.

Experimental (**A–D**) Q-band HYSCORE spectra of **1edt** measured at the indicated field positions, and corresponding simulations (**E–H**) that account for one ^{57}Fe HF coupling (**A**(Fe$_2$), Table 1). Experimental conditions: T = 20 K; τ = 420 n; ν_{mw} = 33.8883 GHz; $t(\pi/2)$ = 40 ns; $\Delta T_{1,2}$ = 52 ns.

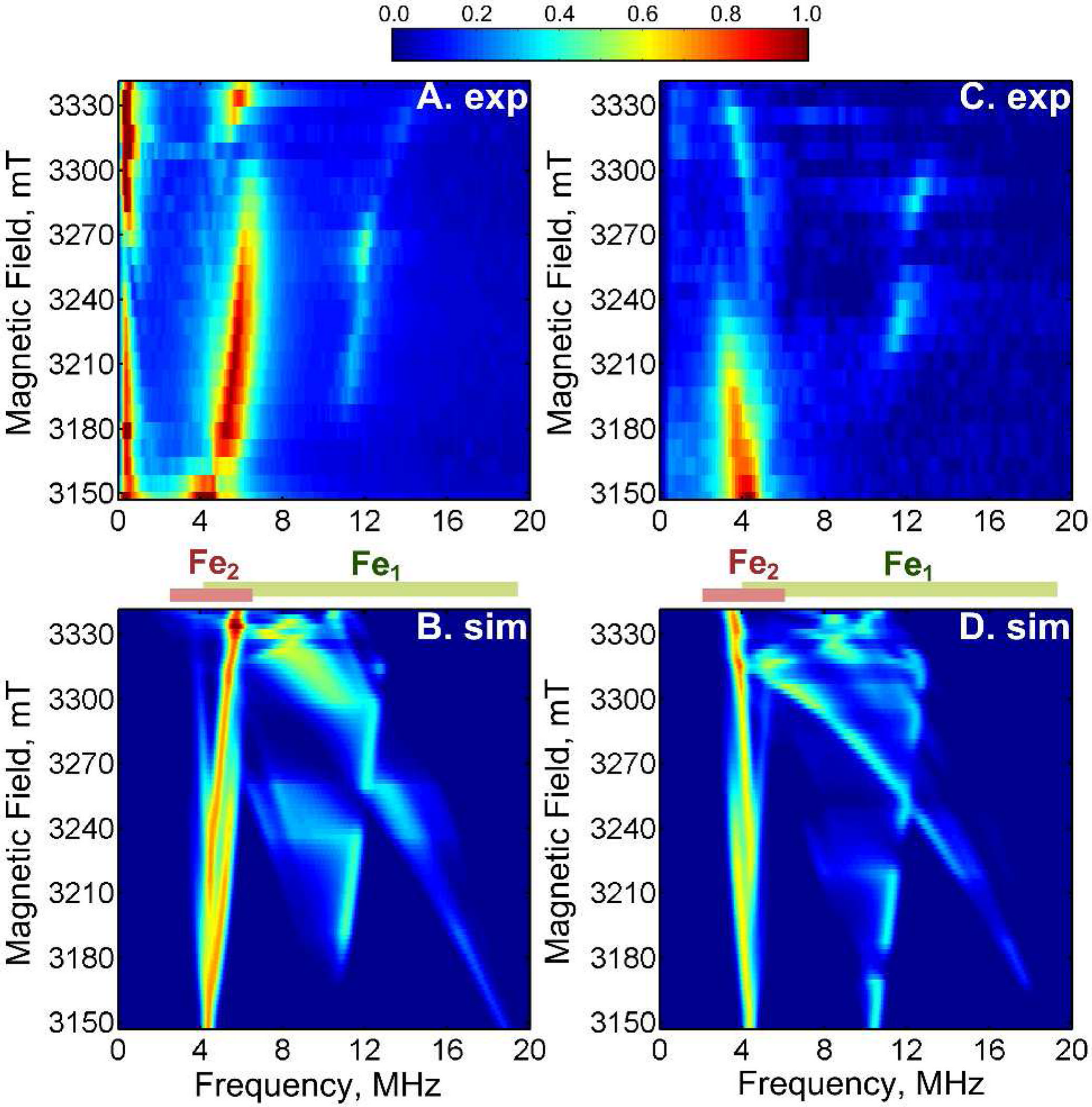

Figure 7.

W-band 3-pulse ESEEM spectra as function of the applied magnetic field B_0 of ^{57}Fe-enriched **1edt**, measured at two different τ-values: 164 ns (**A**) and 288 ns (**C**), together with the respective simulations (**B, D**) accounting for two contributing ^{57}Fe HF couplings (Table 1). Experimental conditions: T = 10 K; τ = 164 ns; ν_{mw} = 94.0928 GHz; $t(\pi/2)$ = 24 ns; ΔT = 12 ns. The color coding of the signal relative intensity is represented by the color bar.

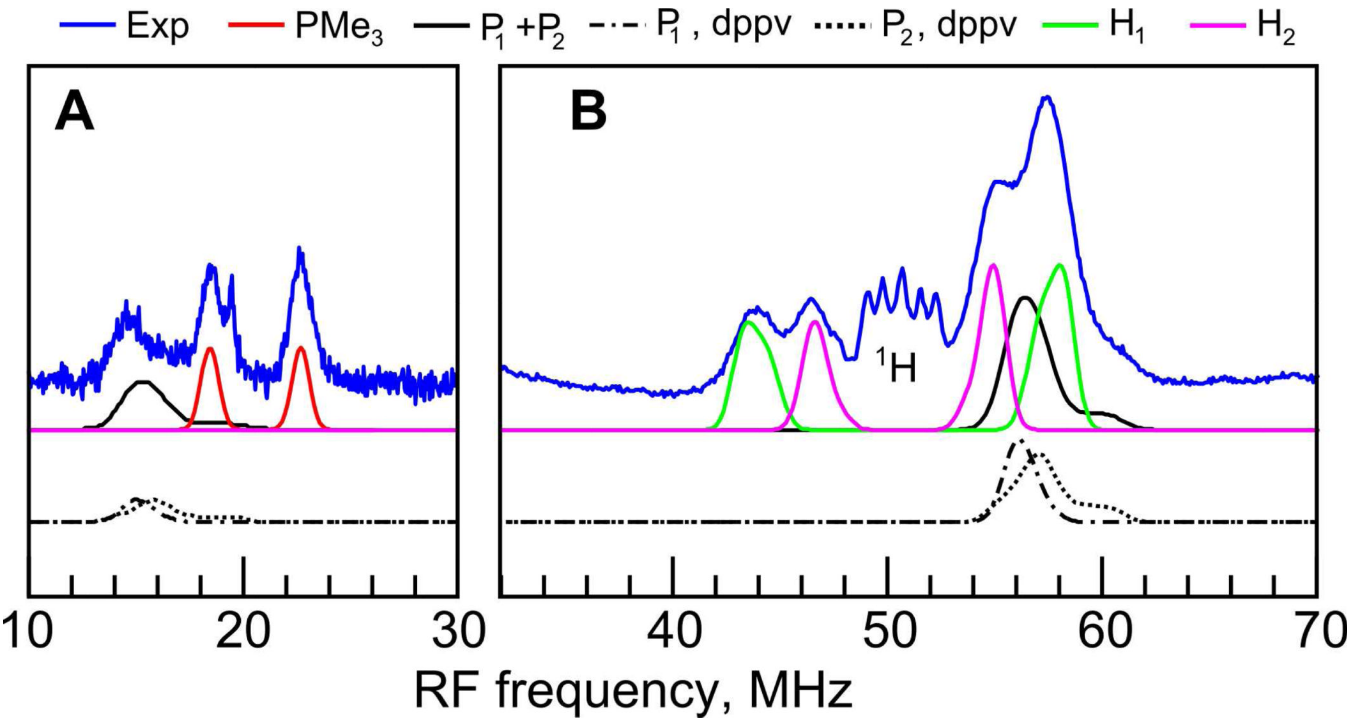

Figure 8.

Q-band ENDOR spectra of **1adt** measured at 20 K and field position 1192.8 mT (g_y). Low frequency spectra (**A**) were recorded using the refocused Mims ENDOR sequence with τ = 108 ns and $t(\pi/2)$ = 16 ns, whereas the high frequency part (**B**) was recorded using Davies ENDOR, t_{inv} = 44 ns (suppressing matrix ^{1}H signals), $t(\pi/2)$ = 16 ns, τ = 400 ns. Simulations were performed using the HF coupling constants listed in Table 1. See also Figure S3 in SI for complete field dependence.

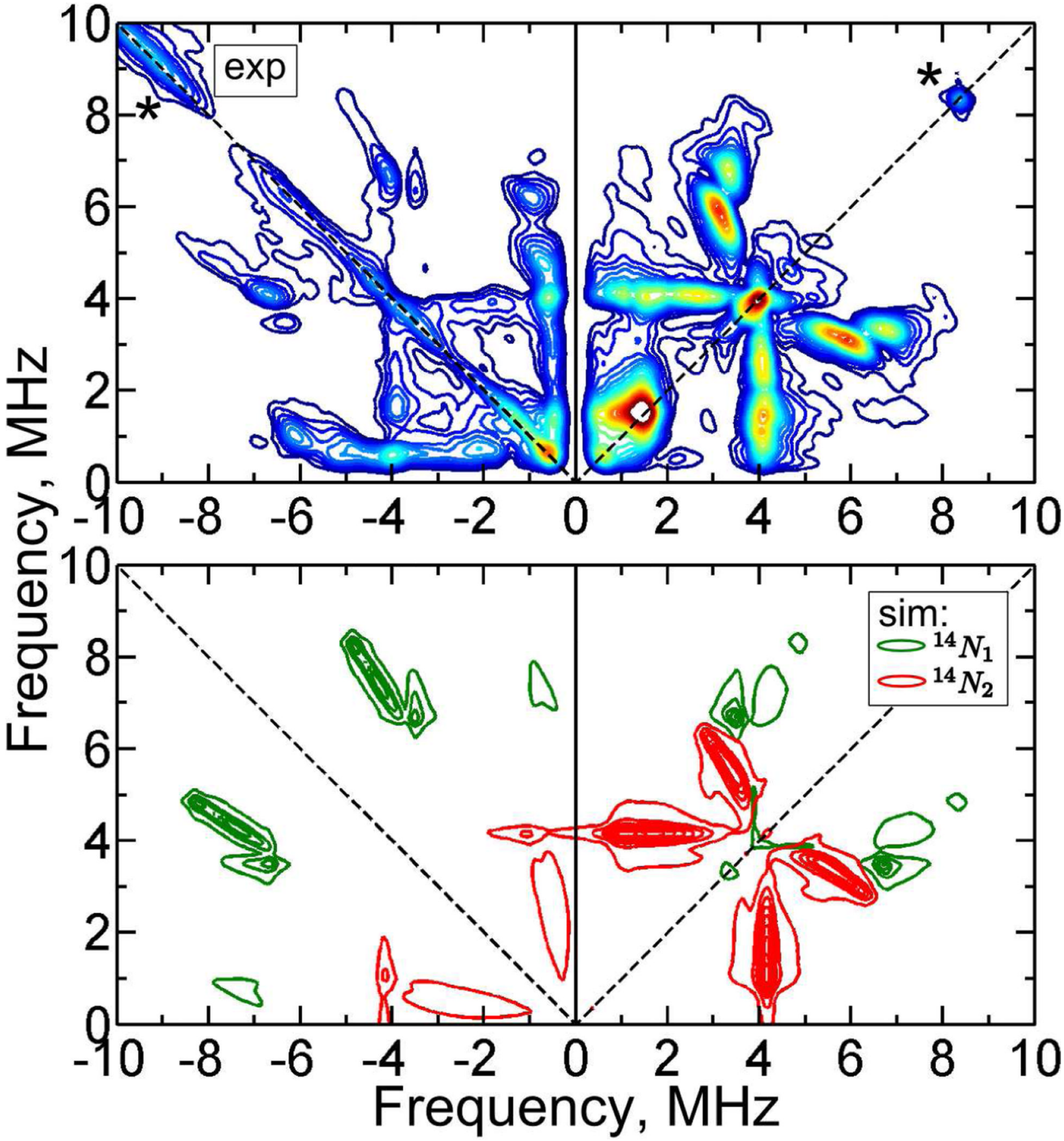

Figure 9.

X-band HYSCORE spectra of **1adt** (top) and corresponding simulations (bottom) accounting for two independent ^{14}N signals that correspond to two isomeric forms of the amine group (see also Figure S6). Experimental parameters: $B_0 = 342.5$ mT; T = 20 K; $\nu_{mw} = 9.720$ GHz; $t(\pi/2) = 8$ ns; $\tau = 86$ ns. For clarity the presented spectra are cropped to the low frequency range, neglecting the ^{1}H signals. Asterisks denote instrumental artifacts.

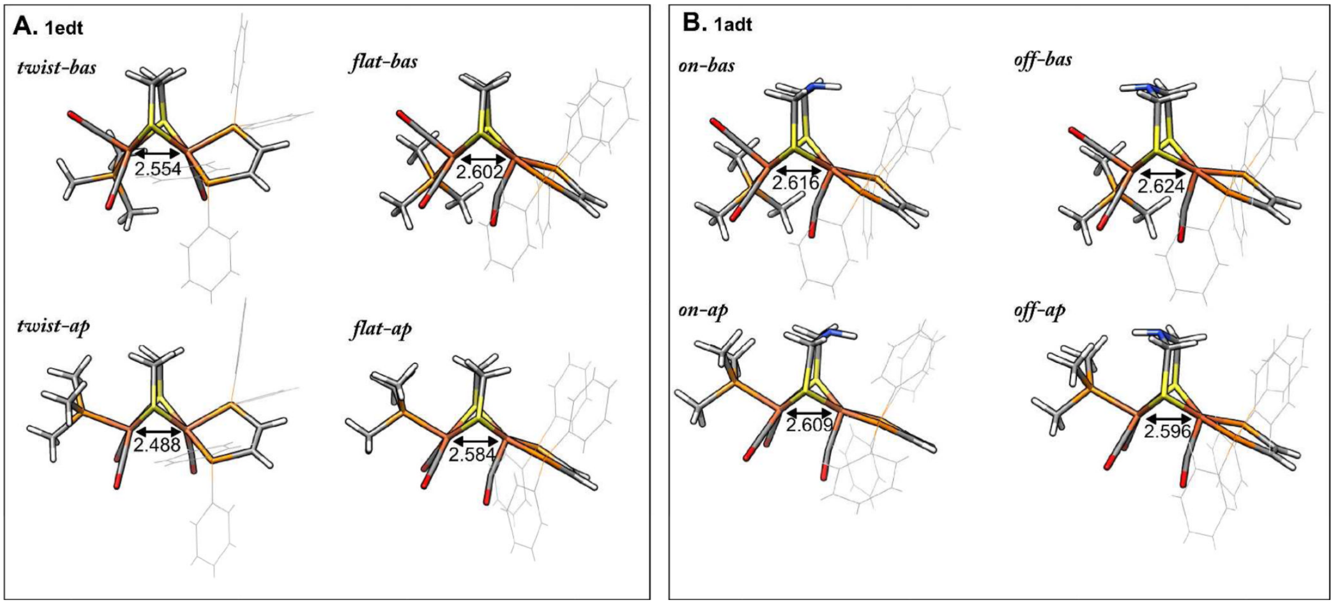

Figure 10.

Geometry optimized isomers of **1edt** (**A**) and **1adt** (**B**). Fe_1-Fe_2 distances are indicated in Å. "bas"/"ap" stands for basal or apical position of the PMe_3 ligand, respectively. "flat"/"twist" stands for flat (square-pyramidal) configuration of dithiolate and dppv ligands and twisted configuration. "on"/"off" indicate the position of the amine with respect to the dppv ligand.

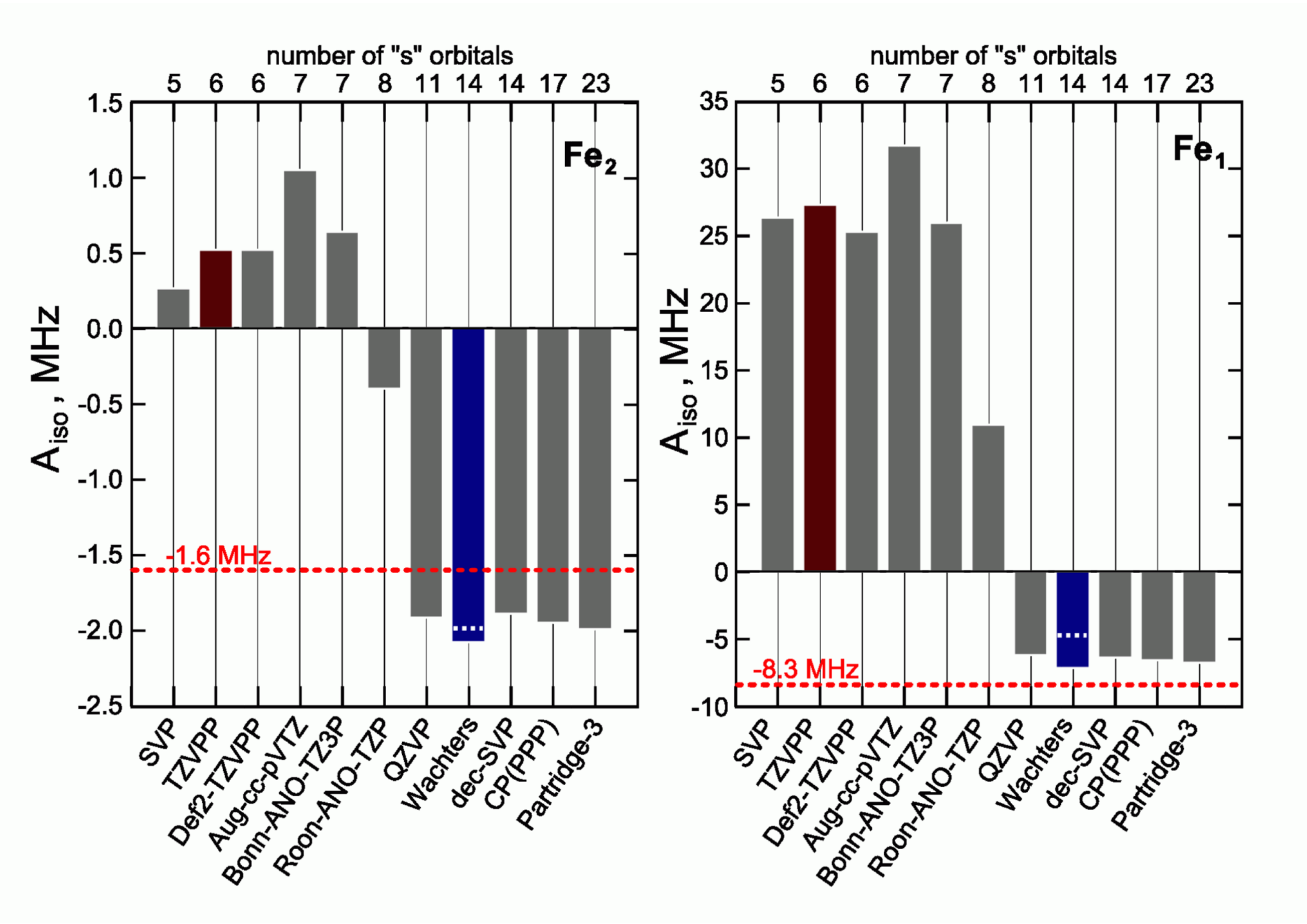

Figure 11.

^{57}Fe A_{iso} coupling constants of **1edt$_{\textbf{flat-bas}}$** as calculated using various basis sets (see Supporting Information for detailed description) in conjunction with the B3LYP functional and TZVPP basis set on all other atoms not taking into account second order spin orbit coupling contributions. The red dashed lines indicate the experimentally obtained values from Table 1. Brown and blue bars identify TZVPP and Wachters basis sets, respectively. The white dashed lines in the blue bars indicate spin-orbit coupling corrections to the isotropic hyperfine coupling.

Table 1

Principal HFI tensor values (MHz) for **1edt** and **1adt** obtained from simulations of experimental spectra.

Nucleus (assignment)	A_x	A_y	A_z	$A^{a)}_{iso}$	Euler angles (deg)		
					α	β	γ
1edt							
$^{31}P_1$ (dppv)	−72	−71	−80	−74.3	0	30	0
$^{31}P_2$ (dppv)	−73	−72	−85	−76.6	0	30	0
$^{31}P_3$ (PMe_3)	−9.5	−11.0	−8.5	−9.7	0	40	0
^{57}Fe (Fe_1)	−12.0	+16.6	−29.5	−8.3	10	10	0
^{57}Fe (Fe_2)	−3.0	−1.0	+0.5	−1.16	0	15	20
1adt							
$^{31}P_1$ (dppv)	−70	−71	−78	−73.0	0	30	0
$^{31}P_2$ (dppv)	−69	−72	−85	−75.3	0	30	0
^{31}P (PMe_3)	−4.3	−4.5	−3	−3.90	0	30	0
$^{14}N_1$[b)]	+5.4	+3.7	+3.0	+4.0	10	25	0
$^{14}N_2$[b)]	+0.0	+0.0	+3.5	+1.17	30	60	0
$^{1}H_1$	+11.1	+15.8	+13.5	+13.4	40	30	0
$^{1}H_2$	+5.0	+8.5	+10.5	+8.0	30	30	0

[a)] $A_{iso} = (A_x + A_y + A_z)/3$

[b)] sign of the HF coupling is assumed based on DFT calculations (vide infra).

Table 2

^{57}Fe Quarupole and Isomer Shift Parameters obtained from Mössbauer Data for 1edt.

Nucleus	**ΔE_Q (mm/s)**	**η**	**δ (mm/s)**	**Euler Angles (deg.)**		
				A	**β**	**γ**
^{57}Fe (Fe_1)	−0.58(3)	+0.90(10)	+0.20(1)	20	60	0
^{57}Fe (Fe_2)	+0.70(3)	+0.92(10)	+0.04(1)	0	−10	0

Table 3

^{14}N Quadrupole Parameters obtained from X-band HYSCORE Analysis of 1adt.

	K(MHz)	**η**	**Euler Angles (deg.)**		
			α	**β**	**γ**
$^{14}N_1$	1.12(1)	+0.20(5)	10	20	0
$^{14}N_2$	1.15(1)	0.00(10)	0	70	0

Table 4

Comparison of experimental and calculated parameters for **1edt**

	twist-ap	**twist-bas**	**flat-ap**	**flat-bas**	**exp**
Δ*E*, kcal/mol	5.73	5.76	2.03	0.00	-
^{57}Fe, Fe$_1$[a)]					
A_{iso} (MHz)	−0.55	+0.97	−4.59	−4.74	−8.30
A_{dip} (MHz)	+11.14	+9.64	+15.97	+16.58	+12.45
A_{rh}	+0.68	+0.99	+0.46	+0.35	+ 0.70
ΔE_Q (mm/s)[b)]	+1.47	−1.17	−0.41	−0.49	−0.58
η	0.87	0.87	0.91	0.97	0.90
δ (mm/s)[c)]	+0.15	+0.14	+0.17	+0.16	+0.20
Mulliken	0.7448	0.7023	0.9740	1.0189	
^{57}Fe, Fe$_2$[a)]					
A_{iso} (MHz)	−0.57	0.55	−2.25	−1.99	−1.16
A_{dip} (MHz)	+5.77	+7.17	+2.02	+1.43	+0.90
A_{rh} (MHz)	+0.64	+0.79	+0.30	+0.23	+0.82
ΔE_Q (mm/s)[b)]	+0.70	−0.59	+0.67	+0.80	+0.70
η	0.99	0.69	0.52	0.48	0.92
δ (mm/s)[c)]	−0.03	−0.01	+0.01	+0.01	+0.04
Mulliken	0.3946	0.4178	0.1147	0.0797	
^{31}P(dppv), A$_{iso}$ (MHz)					
P_1	−66.85	−60.13	−85.17	−82.29	−74.3
P_2	−60.78	−58.69	−84.39	−85.70	−76.6
^{31}P(PMe$_3$), A$_{iso}$ (MHz)					

	twist-ap	twist-bas	flat-ap	flat-bas	exp
P_3	+8.15	−40.22	+6.10	−11.91	−9.70

[a] A_{iso} - isotropic part, A_{dip} - magnitude of the anisotropic part, A_{rh} - rhombicity of anisotropic part, i.e. degree of deviation from axial character as such: $A = A_{iso} + A_{dip}[-1+A_{rh}, -1-A_{rh}, 2]$

[b] As the asymmetry parameter is almost 100% the sign of ΔE_Q does not have a physical meaning

[c] $\delta = 0.1181 - 0.3821 (\rho (0) - 11614)$, see Materials and Methods.

Table 5

Comparison of experimental and calculated parameters for **1adt**.

	on-ap	**on-bas**	**off-ap**	**off-bas**	**exp**[c)]
ΔE, kcal/mol	2.79	0.00	4.16	0.32	-
^{14}N(adt)[a)]					
A_{iso} (MHz)	+3.92	+2.91	+0.59	+0.83	+4.00 /+ 1.17
A_{dip} (MHz)	+0.21	+0.22	+0.66	+0.72	+0.68 /+ 1.17
A_{rh}	+0.34	+0.24	+0.03	+0.03	+0.51 /+ 0.0
K (MHz)	−1.24	−1.25	−1.24	−1.22	1.12 / 1.15
η	0.09	0.07	0.07	0.11	0.20 / 0.0
^{31}P(dppv), A_{iso} (MHz)					
P_1	−88.27	−83.85	−86.23	−82.08	−73.0
P_2	−92.01	−88.30	−86.22	−87.38	−75.3
^{31}P(PMe$_3$), A_{iso} (MHz)					
P_3	+8.39	−9.61	+9.59	−6.67	−3.90
^{1}H(adt) A_{iso} (MHz)[b)]					
H_1	+2.68	+1.37	+7.05	+4.95	+8.30
H_2	+1.95	+1.78	+7.07	+7.67	+13.50
H_3	−1.30	−0.81	−0.87	−1.19	-
H_4	−1.32	−0.77	−1.07	−1.00	-
^{1}H(NH), A_{iso} (MHz)					
H_5	−0.60	−0.41	−1.07	−0.92	-

[a)] A_{iso} - isotropic part of HF coupling, A_{dip} - magnitude of the anisotropic part, A_{rh} - rhombicity of anisotropic part, i.e. degree of deviation from axial character as such: $A = A_{iso} + A_{dip}[-1+A_{rh}, -1-A_{rh}, 2]$.

[b] For assignment of ^{1}H HFCs, see Figure S11

[c] If no sign is given it is not determined experimentally.